

# Human XPR1 structures reveal phosphate export mechanism

<https://doi.org/10.1038/s41586-024-07852-9>

Received: 28 November 2023

Accepted: 18 July 2024

Published online: 21 August 2024

 Check for updates

Rui Yan<sup>1,2,6</sup>, Huiwen Chen<sup>1,3,6</sup>, Chuanyu Liu<sup>1,4,6</sup>, Jun Zhao<sup>5,6</sup>, Di Wu<sup>1,4</sup>, Juquan Jiang<sup>3</sup>, Jianke Gong<sup>2</sup> & Daohua Jiang<sup>1,4</sup>✉

Inorganic phosphate (Pi) is a fundamental macronutrient for all living organisms, the homeostasis of which is critical for numerous biological activities<sup>1–3</sup>. As the only known human Pi exporter to date, XPR1 has an indispensable role in cellular Pi homeostasis<sup>4,5</sup>. Dysfunction of XPR1 is associated with neurodegenerative disease<sup>6–8</sup>. However, the mechanisms underpinning XPR1-mediated Pi efflux and regulation by the intracellular inositol polyphosphate (InsPP) sensor SPX domain remain poorly understood. Here we present cryo-electron microscopy structures of human XPR1 in Pi-bound closed, open and InsP<sub>6</sub>-bound forms, revealing the structural basis for XPR1 gating and regulation by InsPPs. XPR1 consists of an N-terminal SPX domain, a dimer-formation core domain and a Pi transport domain. Within the transport domain, three basic clusters are responsible for Pi binding and transport, and a conserved W573 acts as a molecular switch for gating. In addition, the SPX domain binds to InsP<sub>6</sub> and facilitates Pi efflux by liberating the C-terminal loop that limits Pi entry. This study provides a conceptual framework for the mechanistic understanding of Pi homeostasis by XPR1 homologues in fungi, plants and animals.

Phosphorus is an essential element for all domains of life and is involved in bone and tooth growth, biogenesis of lipids and nucleic acids, high-energy organic compound metabolism and protein signalling<sup>1,2</sup>. Cellular Pi levels are tightly regulated to match the biosynthetic demand for Pi and to avoid excessive cytosolic Pi levels; dysregulation of Pi homeostasis causes pathological consequences<sup>3,9</sup>. In mammals, cells take up Pi from the extracellular space through the PiT (also known as SLC20A) and NPT2 (also known as SLC34A) transporters<sup>10–12</sup>. Conversely, as the only known Pi exporter in mammals to date, xenotropic and polytropic retrovirus receptor 1 (XPR1; encoded by *SLC53A1*) mediates Pi efflux in response to elevated intracellular Pi levels<sup>4,5,13</sup>, thereby having a crucial role in maintaining cellular Pi homeostasis<sup>14</sup>. Deletion of the gene encoding XPR1 in mice is lethal<sup>15</sup>, and loss-of-function mutations of XPR1 are associated with human neurological disease primary familial brain calcification (PFBC) and renal Fanconi syndrome<sup>6–8,15,16</sup>. In plants, PHOSPHATE1 (PHO1) loads Pi from the roots to the shoots<sup>17,18</sup>, having an indispensable role in plant Pi homeostasis and signalling<sup>19</sup>. In yeast, SYG1 is an orthologue of XPR1 and PHO1 and is considered a putative Pi exporter<sup>4</sup>. The three proteins share a sequence identity of approximately 25% and exhibit a conserved topology of an N-terminal SPX (SYG1, PHO1, XPR1) domain and a following transmembrane domain (TMD). The TMD consists of ten transmembrane helices, of which the six transmembrane helices of the C terminus are named the EXS (Erd1, XPR1, SYG1) domain<sup>20</sup> and are crucial for Pi transport<sup>21</sup>. The SPX domain-containing proteins are widely distributed in fungi, plants and metazoans and have been implicated as an inositol polyphosphate (InsPP) sensor<sup>22</sup>, which monitors intracellular InsPPs and regulates cellular Pi levels via Pi transporters or Pi-dependent transcription

factors<sup>22–26</sup>. Although the structures of the conserved SPX domain have been revealed<sup>22,27–29</sup>, the architecture of XPR1 homologues and how the SPX domain communicates with the TMD remain largely unknown.

XPR1 is widely expressed in human tissues<sup>4</sup> and was initially identified as a receptor for xenotropic and polytropic murine leukaemia viruses<sup>30–32</sup>. Studies have demonstrated that XPR1 mediates Pi efflux<sup>4,13</sup>. Although XPR1 retains Pi export activity without the SPX domain<sup>4</sup>, its function can be enhanced by the SPX domain, which senses intracellular InsPPs including 1,5-InsP<sub>8</sub> (ref. 5). Increased cytosolic Pi levels result in accumulation in InsPPs, which in turn bind to the SPX domain and facilitate Pi efflux via XPR1 to balance cellular Pi levels<sup>5</sup>. However, the underlying mechanisms of how XPR1 recognizes and transports Pi and how this process is regulated by the SPX domain remain undefined. In this study, we determined the cryo-electron microscopy (cryo-EM) structures of human XPR1 in three distinct functional states with bound Pi and inositol hexakisphosphate (InsP<sub>6</sub>), demonstrating the structural features and Pi export mechanism of XPR1-like proteins. Complemented with functional mutagenesis results, this study elucidates critical insights into Pi binding, gating, InsPP sensing, and the coupling between InsPP sensing and Pi export in XPR1, which are vital for human Pi homeostasis.

## Structural determination of XPR1

We overexpressed human full-length wild-type XPR1 (XPR1<sup>WT</sup>) in HEK293T cells and assayed its Pi export activity. In line with previous studies<sup>4,16</sup>, XPR1-expressing cells exhibited robust Pi efflux, which is approximately 2.5-fold of the basal level of HEK293 cells transfected

<sup>1</sup>Laboratory of Soft Matter Physics, Institute of Physics, Chinese Academy of Sciences, Beijing, China. <sup>2</sup>College of Life Science and Technology, Key Laboratory of Molecular Biophysics of MOE, Huazhong University of Science and Technology, Wuhan, China. <sup>3</sup>Department of Microbiology and Biotechnology, College of Life Sciences, Northeast Agricultural University, Xiangfang District, Harbin, China. <sup>4</sup>University of Chinese Academy of Sciences, Beijing, China. <sup>5</sup>Peking University Institute of Advanced Agricultural Sciences, Shandong Laboratory of Advanced Agricultural Sciences at Weifang, Weifang, China. <sup>6</sup>These authors contributed equally: Rui Yan, Huiwen Chen, Chuanyu Liu, Jun Zhao. <sup>✉</sup>e-mail: jiangdh@iphy.ac.cn

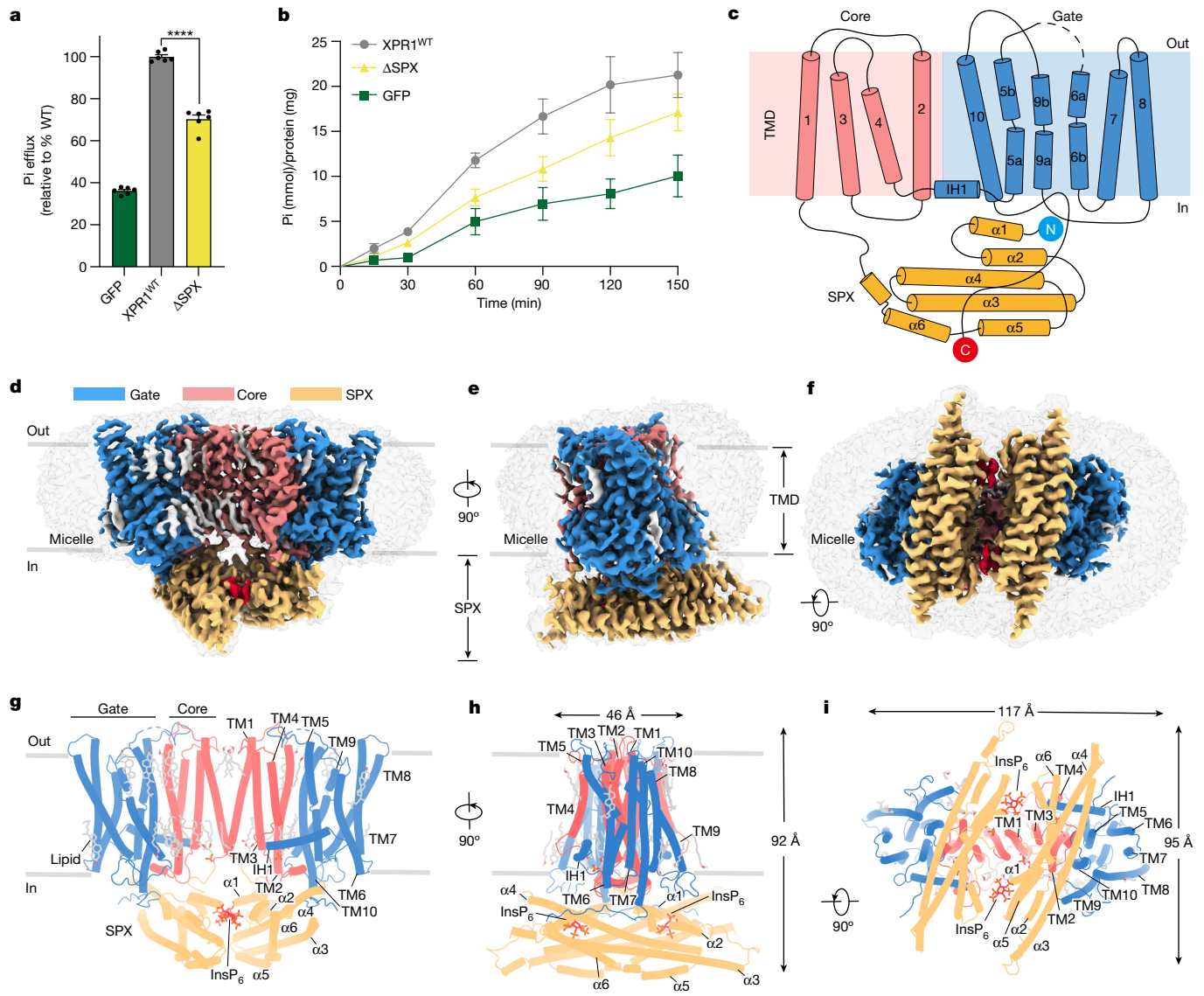


**Fig. 1 | Functional characterization and electron microscopy structure of human XPR1.** **a**, Pi export by XPR1<sup>WT</sup> and XPR1<sup>ΔSPX</sup>. Cells expressing GFP served as controls. Data were normalized to XPR1<sup>WT</sup> and are presented as mean  $\pm$  s.e.m.;  $n = 6$  from three independent replicates. One-way analysis of variance (ANOVA) was used; \*\*\* $P < 0.0001$ . **b**, Time course of Pi export by XPR1<sup>WT</sup> and XPR1<sup>ΔSPX</sup>. Data are presented as mean  $\pm$  s.e.m.;  $n = 3$  independent replicates. **c**, Topology of XPR1. The SPX, core and transport domains are

coloured in yellow, red and blue, respectively. The same colour scheme is applied throughout the paper unless otherwise specified. **d–f**, The electron microscopy map of XPR1<sup>ΔSPX</sup> presented in three different views. Electron microscopy densities for lipids and InsP<sub>6</sub> are coloured in grey and red, respectively. **g–i**, Cartoon representation of XPR1<sup>ΔSPX</sup> presented in the three views from panels **d–f**. The grey sticks indicate lipids, and the red sticks denote InsP<sub>6</sub>. Source Data are provided.

with GFP alone (Fig. 1a). We next generated the SPX domain (2–224) truncated XPR1 (XPR1<sup>ΔSPX</sup>), which exhibits comparable plasma membrane localization and cell-surface expression with those of XPR1<sup>WT</sup> in HEK293T cells (Supplementary Figs. 1 and 2). Although the Pi export activity of XPR1<sup>ΔSPX</sup> was noticeably decreased compared with that of XPR1<sup>WT</sup>, it was still substantially above the basal level (Fig. 1a). We further investigated the time course of Pi efflux by XPR1<sup>WT</sup> and XPR1<sup>ΔSPX</sup>. Within the tested timeline of 150 min, Pi efflux by XPR1<sup>WT</sup> gradually increased to reach a steady stage, whereas XPR1<sup>ΔSPX</sup>-mediated Pi efflux almost linearly increased at a slower pace (Fig. 1b), suggesting a regulatory role of the SPX domain. Consistent with previous studies<sup>4,5</sup>, these Pi export results confirm that the TMD of XPR1 mediates Pi export, which can be regulated by the SPX domain.

To reveal the structural basis for Pi efflux by XPR1, we purified XPR1<sup>WT</sup> samples in phosphate buffer and performed cryo-EM single-particle analysis of the samples (Extended Data Figs. 1–4 and Supplementary

Table 1). Two-dimensional (2D) and 3D classifications showed apparent twofold symmetry within the specimens. The final electron microscopy map was obtained from 253,874 particles at a resolution of 2.84 Å with C<sub>2</sub> symmetry imposed (Extended Data Fig. 2a). The density map facilitates accurate modelling of the TMD of XPR1, ranging from A229 to V626, lipids and phosphate solvents (Extended Data Figs. 5a and 6a). However, no discernible electron microscopy density could be observed for the SPX domain (M1 to P228), presumably because of loose interactions between the TMD and the SPX domain in the absence of InsPPs. To verify the state of heterogeneity in XPR1, we performed local 3D classification with a focused mask covering one TMD region using the particles with symmetry expansion (Extended Data Fig. 2b). Unexpectedly, focused 3D classification yielded a reconstruction map that displayed obvious conformational changes in transmembrane helix 9 (TM9), in sharp contrast to the aforementioned structure (Extended Data Figs. 2b and 6b). Subsequently, a 3.61 Å electron microscopy map was obtained

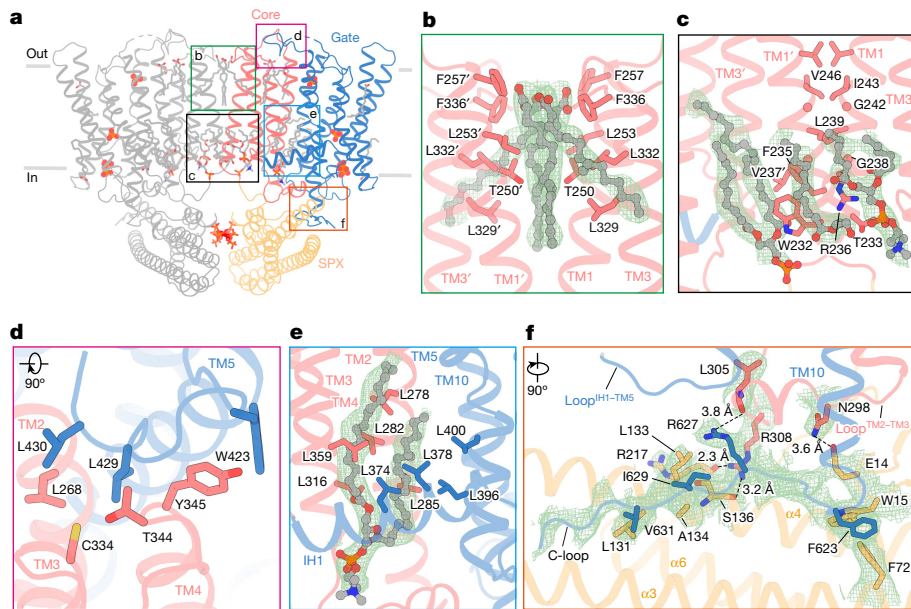


**Fig. 2 | Architecture of human XPR1.** **a**, Overall structure of the XPR1 dimer. The left protomer is coloured in grey. Lipids, Pi ions and  $\text{InsP}_6$  are shown in sticks. The boxes indicate the focused areas shown in panels **b–f**. **b, c**, Zoomed-in view of the dimer interface on the extracellular side (**b**) and the intracellular side (**c**). Residues involved in the dimer interface are shown as side chains in sticks. **d, e**, Interactions in the interface of the core and gate domains on the

extracellular side (**d**) and the intracellular side (**e**). Residues involved in the interface are shown as side chains in sticks. **f**, Interactions between the SPX domain and the C-loop. Residues involved in the interactions are shown as side chains in sticks. The black dashed lines represent polar interactions. All electron microscopy densities in this figure are shown in green meshes and contoured at  $8\sigma$ .

(Extended Data Figs. 3b and 5b), which allowed model building of a second XPR1 structure (Extended Data Fig. 6b). These two structures are termed  $\text{XPR1}^{\text{Closed}}$  and  $\text{XPR1}^{\text{Open}}$ , respectively.

To further reveal the full-length structure, XPR1 samples were purified similarly with the addition of 1 mM  $\text{InsP}_6$  and analysed by cryo-EM (Extended Data Figs. 1b and 4). Of note, apparent electron microscopy densities for the SPX domain emerged from the 2D and 3D classifications (Extended Data Fig. 4a). The final electron microscopy map was determined from 30,798 particles at a resolution of  $2.96\text{ \AA}$  (Extended Data Fig. 4b–d). The electron microscopy map permits reliable model building of XPR1 (M1 to N635), including the SPX domain, TMD, C-terminal loop (C-loop), lipids and  $\text{InsP}_6$ , resulting in a third structure:  $\text{XPR1}^{\text{InsP}_6}$  (Fig. 1d–i).

## Architecture of XPR1

The three structures of  $\text{XPR1}^{\text{Closed}}$ ,  $\text{XPR1}^{\text{Open}}$  and  $\text{XPR1}^{\text{InsP}_6}$  display a high degree of structural similarity in the TMD region, although TM9 of  $\text{XPR1}^{\text{Open}}$  and the SPX domain and the C-loop of  $\text{XPR1}^{\text{InsP}_6}$  adopt different conformations (Extended Data Fig. 6). Because the  $\text{XPR1}^{\text{InsP}_6}$  structure is more complete, we describe the structural features of XPR1 using this structure. The XPR1 structure is organized in a homodimeric manner with dimensions of  $117\text{ \AA} \times 92\text{ \AA} \times 95\text{ \AA}$  (Fig. 1g–i). Each protomer consists of an N-terminal SPX domain, ten transmembrane helices (TM1–10), an amphipathic intracellular helix (IH1) and a C-loop (Fig. 1c). The TMD comprises two structural units: a ‘core’ domain formed by helices TM1–4 defining the dimer interface, and a ‘gate’ domain formed by helices TM5–10 that are responsible for Pi transport (Fig. 1c,g). The SPX domain is positioned below the TMD parallel to the membrane plane and perpendicular to the TMD (Fig. 1d–i). Similar dimer-form and two-domain organization have been revealed in other SLC transporters<sup>33–35</sup>. However, XPR1 exhibits unique structural features and arrangement (Fig. 1c–i). The XPR1 structure exhibits similarity to the AlphaFold2 (ref. 36) models of human XPR1 (root-mean-square deviation (RMSD) at  $1.75\text{ \AA}$  over 583  $C\alpha$  atoms), yeast *Saccharomyces*

*cerevisiae* SYG1 (RMSD at  $3.15\text{ \AA}$  over 412  $C\alpha$  atoms) and plant *Arabidopsis thaliana* PHO1 (RMSD at  $1.82\text{ \AA}$  over 534  $C\alpha$  atoms; Extended Data Fig. 7a–c), suggesting that these XPR1 homologues in fungi and plants should assume similar architecture to XPR1.

The dimer interface is formed by the SPX domain and TM1 of the core domain, covering solvent-accessible surface areas of  $146\text{ \AA}^2$  and  $601\text{ \AA}^2$ , respectively (Fig. 2a). Broad hydrophobic interactions were observed between the two TM1 helices with contributions from multiple lipid molecules (Fig. 2b,c), suggesting that lipids may have a role in the dimer formation, consistent with the observation of lipid molecules in the dimeric interface of other SLC transporters<sup>34,37,38</sup>. To assess the role of TM1 in dimer formation and function, we substituted G238 and G242 with a phenylalanine, respectively, which could bring steric hindrance to the dimer interface (Supplementary Fig. 3a). The G238F and G242F mutants exhibited greatly impaired Pi export activities and a monomer peak in solution distinct from the dimer peak of  $\text{XPR1}^{\text{WT}}$  from the fluorescence-detection size-exclusion chromatography (FSEC) profiles (Supplementary Fig. 3b,c), indicating that the dimeric form is functionally required. In addition, two SPX domains are arranged in an antiparallel manner, with two  $\text{InsP}_6$  molecules between the dimer interface that may contribute to stabilizing the XPR1 dimer (Figs. 1i and 2a). However, the  $\text{XPR1}^{\text{Closed}}$  structure exhibits a virtually identical dimer interface in the TMD to that of  $\text{XPR1}^{\text{InsP}_6}$ , despite its SPX domain not being visible (Extended Data Fig. 6a,e). We investigated the molar mass of purified  $\text{XPR1}^{\text{WT}}$  and  $\text{XPR1}^{\text{ASPX}}$  in detergent solution by SEC coupled with multi-angle light scattering, generating a molar mass of 166 kDa for  $\text{XPR1}^{\text{WT}}$  and of 107 kDa for  $\text{XPR1}^{\text{ASPX}}$  (Extended Data Fig. 1d), indicating that both  $\text{XPR1}^{\text{WT}}$  and  $\text{XPR1}^{\text{ASPX}}$  are in a dimeric form. Consistent with the structural observation, these findings suggest that the interactions between the TMDs are the main determinants of XPR1 dimerization.

The core domain serves as a scaffold for the gate domain (Fig. 2a). The two domains are connected by the amphipathic IH1 and form multiple hydrophobic interactions (Fig. 2d,e). In particular, TM2, IH1 and TM5 form a triangle-shaped hydrophobic cavity filled with a putative

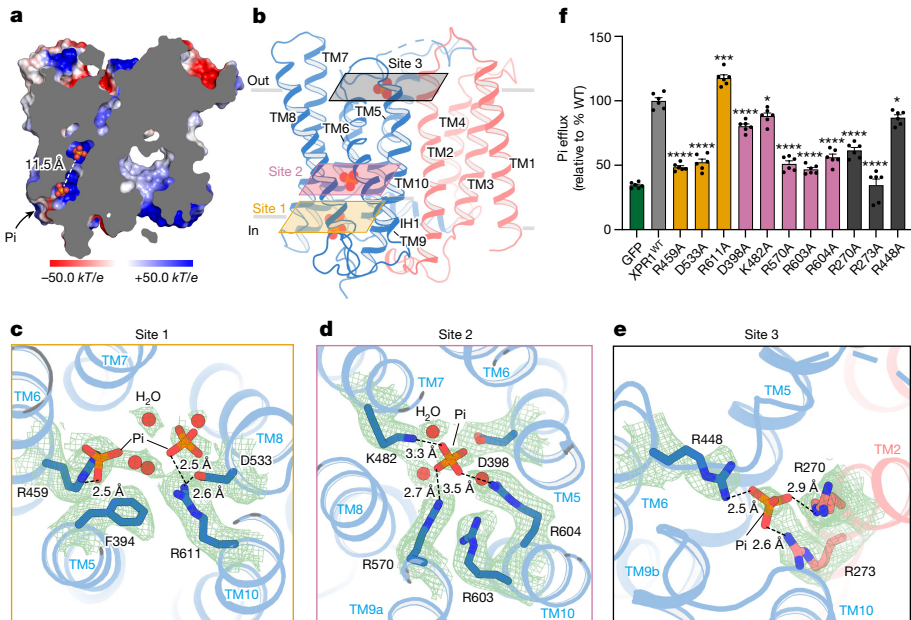


**Fig. 3 | Structural basis for Pi binding in XPR1.** **a**, Cut-open sliced electrostatic surface potential of the pore of XPR1<sup>Closed</sup>. Pi is in red spheres. The positive and negative potentials are coloured in blue and red, respectively. The black arrow indicates the entry for Pi. The white dashed lines indicate the distance between Pi bound in sites 1 and 2. **b**, Three Pi-binding sites in the gate domain of XPR1<sup>Closed</sup>. Pi is in red spheres. The yellow, red and black planes indicate each Pi site highlighted in panels **c–e**. **c–e**, Detailed Pi-binding sites in XPR1 for site 1 (**c**), site 2 (**d**) and site 3 (**e**). Pi molecules and residues that contributed to Pi binding are shown in sticks. The red balls represent putative water molecules. Electron

microscopy densities for the residues, Pi and water molecules are shown in green meshes and contoured at 5σ. The black dashed lines represent electrostatic interactions. **f**, Pi export activities of XPR1<sup>WT</sup> and variants with single-site mutations involved in Pi binding. Cells expressing GFP served as controls. Data were normalized to XPR1<sup>WT</sup> and are presented as mean ± s.e.m.;  $n = 6$  from three independent replicates. One-way ANOVA was used; \* $P = 0.045$  for K482A, \* $P = 0.017$  for R448A, \*\*\* $P < 0.001$  and \*\*\*\* $P < 0.0001$ . Source Data are provided.

phospholipid molecule (Fig. 2e). The TM5–10 helices are arranged in a clockwise manner viewed from the intracellular side to form the gate domain (Fig. 1i), which has a highly positively charged pore that facilitates Pi binding and translocation (Fig. 3a). In line with this, the gate domain corresponds to the EXS domain, which has been suggested to be responsible for Pi export in PHO1 (refs. 20,21).

The SPX domain is formed by six α-helices (α1–6) into a helical bundle, which closely resembles the reported structures of SPX domains<sup>22</sup> (Extended Data Fig. 7g–j). In XPR1, SPX is linked to the TMD via a relatively flexible loop (G209–P228) and engages with the intracellular loop between TM2 and TM3 (loop<sup>TM2–TM3</sup>) and the C-loop (Fig. 2a,f). Specifically, N298 forms a hydrogen bond with E14, and R308 engages in electrostatic interactions with the backbone carbonyl oxygen atoms of S136 and R217, respectively (Fig. 2f). In addition, the C-loop lies in a groove of the SPX domain and forms broad polar and hydrophobic interactions such as the stacking of F623 with W15 and F72 (Fig. 2f).

### Pi recognition in XPR1

In our 2.8 Å XPR1<sup>Closed</sup> structure, strong electron microscopy densities revealed several potential phosphate and solvent molecules bound inside the highly hydrophilic pore of the gate domain (Fig. 3a–e). A closer look elucidates that these potential Pi molecules are coordinated by three basic clusters: sites 1–3 (Fig. 3c–e). Site 1 is exposed to the cytosol, in which two possible Pi molecules interact with R459 on TM6 and R611 on TM10, respectively (Fig. 3c). The mutation R459A greatly impaired Pi efflux, and by contrast, R611A substantially increased Pi efflux (Fig. 3f), suggesting that R459 constitutes the intracellular gate for Pi entry. The positively charged R611 is situated outside the gate and may compete with R459 for binding free Pi, thus having a role in regulating Pi efflux activity. Furthermore, the mutation D533A

dramatically decreased Pi export (Fig. 3f), presumably because D533 has a role in neutralizing R611 or providing a repulsion force for Pi accessibility to the intracellular gate (Fig. 3c). Of note, R459A and D533A display markedly reduced cell-surface expression and broad fSEC peaks compared with those of XPR1<sup>WT</sup> (Supplementary Fig. 2c,d,h), suggesting that these mutants could be less stable, and their reduced surface expression contributes to the greatly decreased activity. Site 2 is located approximately 11.5 Å above site 1 in the middle of the membrane bilayer, in which a Pi molecule is cradled by K482 on TM7, R570 on TM9, R603 and R604 on TM10, and D398 on TM5 (Fig. 3a,d). The mutations R570A, R603A and R604A substantially reduced Pi export activities, and D398A and K482A also decreased Pi efflux to a lesser extent (Fig. 3f). The mutations R459C in site 1 and R570C in site 2 have been linked to the human neurological disease PFBC<sup>3,9</sup>. These findings highlight that site 2 functions as a critical Pi-docking site in the Pi translocation pathway. Moreover, site 3 is formed by R270 and R273 on TM2 and R448 on TM6 and is exposed to the extracellular space (Fig. 3b,e). The R273A mutation decreased Pi export activity similar to the control level, and the R270A and R448A mutations also largely impaired Pi export activity (Fig. 3f), indicating that site 3 may provide a positive electrostatic strength that facilitates Pi translocation in XPR1. Similar to R459A in site 1, the R273A mutant has reduced cell-surface expression and a broad fSEC profile (Supplementary Fig. 2b,h), which could be accountable for its negligible activity. Having such dense positively charged residues within the membrane is energetically unfavourable. We observed that multiple negatively charged residues interact with these residues to balance the charges within the membrane (Extended Data Fig. 8a,b). Consistent with this observation, mutations of these charged residues such as R273A, R459A, K482A and D533A could impair the charge balance and lead to protein instability, which may cause their reduced surface expression and broad fSEC profiles (Supplementary Fig. 2b–d,h).

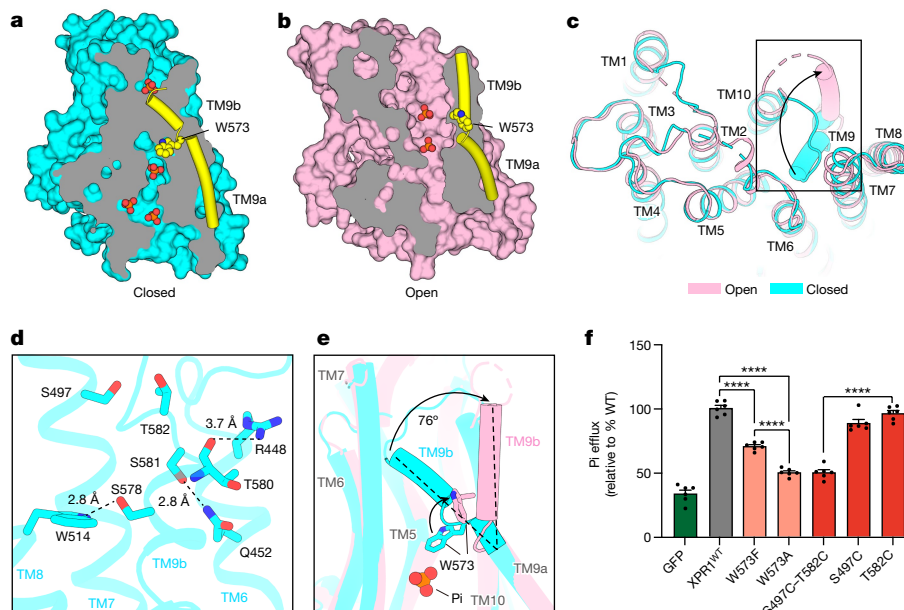


**Fig. 4 | Structural basis for XPR1 gating.** **a,b**, Cut-open surface of XPR1<sup>Closed</sup> (**a**) and XPR1<sup>Open</sup> (**b**). TM9 is shown as a yellow cylinder. Pi molecules and the side chain of W573 are depicted in red and yellow spheres, respectively. **c**, The TMD superposition of XPR1<sup>Open</sup> (pink) and XPR1<sup>Closed</sup> (cyan) viewed from the extracellular side. TM9 is depicted as a cylinder. The black arrow indicates a conformational shift in TM9 between XPR1<sup>Open</sup> and XPR1<sup>Closed</sup>. The black box indicates the focused area shown in panels **d,e**. **d**, Interactions between TM9

and TM6–TM7 in XPR1<sup>Closed</sup>. The black dashed lines represent polar interactions. **e**, Conformational shift in TM9b between XPR1<sup>Open</sup> and XPR1<sup>Closed</sup>. The black arrows indicate the rotation of TM9b and W573. The side chain of W573 is depicted in sticks. **f**, Pi export activities of XPR1<sup>WT</sup> and variants with mutations in TM9. GFP-expressing cells serve as controls. Data were normalized to XPR1<sup>WT</sup> and are presented as mean  $\pm$  s.e.m.;  $n = 6$  from three independent replicates. One-way ANOVA was used; \*\*\* $P < 0.0001$ . Source Data are provided.

Sequence alignments demonstrate that the key residues in sites 1 and 2 are strictly conserved not only in metazoan XPR1 homologues but also in yeast SYG1 and *A. thaliana* PHO1 (Extended Data Figs. 7d,e and 9), highlighting the conserved functional role of sites 1 and 2 in Pi recognition and binding. However, the residues in site 3 are conserved in metazoan XPR1 homologues but not in SYG1 or PHO1 (Extended Data Figs. 7f and 9). R568 and H569 of PHO1 are positioned in similar positions to R448 and R273 in XPR1, respectively (Extended Data Fig. 7f), suggesting that these two residues in PHO1 may compensate for the non-conserved charged residues in site 3. These observations confirm that the gate domain, previously known as the EXS domain<sup>20</sup>, is responsible for Pi translocation in XPR1 homologues.

### Gating mechanism of XPR1

Although the three Pi sites were clearly revealed in the gate domain of XPR1<sup>Closed</sup>, the pore is closed by TM9 (Fig. 4a); by contrast, XPR1<sup>Open</sup> exhibits a continuous translocation pathway within the gate domain that connects the extracellular and intracellular sides (Fig. 4b). Pore radius analysis revealed a tight constriction site of less than 1 Å at W573 in XPR1<sup>Closed</sup> that precludes Pi or other solvents from passing through it, and an expanded pore of more than 2 Å in XPR1<sup>Open</sup> with two constriction sites at sites 1 and 2 (Extended Data Fig. 8c–e). Except for sites 1 and 2 that are responsible for coordinating Pi (Fig. 3c,d), most regions in the open pore are wide enough for conducting Pi (ionic radius of approximately 2.3 Å).

To reveal the transport mechanism for XPR1, we compared the TMDs of XPR1<sup>Closed</sup> and XPR1<sup>Open</sup>, which shows that although most transmembrane helices retain unchanged conformations, TM9 underwent a dramatic conformational shift on the extracellular side (Fig. 4a–c). In XPR1<sup>Closed</sup>, TM9 is inclined to TM6 and TM7 and forms multiple polar interactions with nearby residues from TM6 and TM7 on the extracellular side (Fig. 4d), leading to the closed pore. In XPR1<sup>Open</sup>, TM9 is broken into TM9a and TM9b at W573, of which TM9b is rotated away from the

pore by approximately 76°, resulting in an open pore (Fig. 4e). To assess the observed gating role of TM9b in XPR1, we generated the mutations S497C, T582C and S497C–T582C, which are placed at a suitable distance to form a cysteine disulfide bond in XPR1<sup>Closed</sup> (Fig. 4d). The single-site mutants S497C and T582C showed normal Pi export activities similar to that of XPR1<sup>WT</sup>, but the double mutation S497C–T582C dramatically reduced Pi export activity (Fig. 4f), presumably because the formation of a disulfide bond locks XPR1 in the closed form.

W573 is strictly conserved in SYG1, PHO1 and other XPR1 homologues (Extended Data Fig. 9). To further substantiate the role of W573 in Pi export, we investigated the Pi export activity of W573F and W573A. The W573A mutation greatly impaired XPR1 activity; however, the W573F mutant retained substantial Pi export activity. It is worth noting that W573 is positioned on the top of the Pi bound in site 2 at a distance of 3.7 Å in XPR1<sup>Closed</sup> and rotates its side chain away from the pore in XPR1<sup>Open</sup> (Fig. 4e). On the basis of these findings, we propose that W573 serves as a molecular switch for XPR1 gating, which can be triggered by Pi binding at site 2 and undergoes conformational changes to open the gate. This gating mechanism elucidates that it only requires local conformational changes in TM9b to form a continuous pathway for translocating Pi, demonstrating a unique channel-like transport mechanism that is distinct from the canonical ‘elevator’ or ‘rocker-switch’-like alternating-access mechanism of most transporters<sup>40</sup>.

### Regulation of Pi efflux by the SPX domain

The SPX domain acts as an InsP<sub>6</sub> sensor and has a central role in regulating Pi homeostasis<sup>3,22</sup>. Our XPR1<sup>InsP<sub>6</sub></sup> structure clearly reveals the binding of one InsP<sub>6</sub> molecule to each of the SPX domains (Fig. 5a and Extended Data Fig. 5e). More precisely, InsP<sub>6</sub> is situated in a pocket formed by α1, α2 and α4, and engages in electrostatic interactions and hydrogen bonds with K2, Y22, K26, Y30, R157, K158, K161, K162 and K165 (Fig. 5a). This InsP<sub>6</sub>-binding site is highly conserved in XPR1 homologues and is consistent with the findings of a previous study<sup>22</sup> (Extended Data

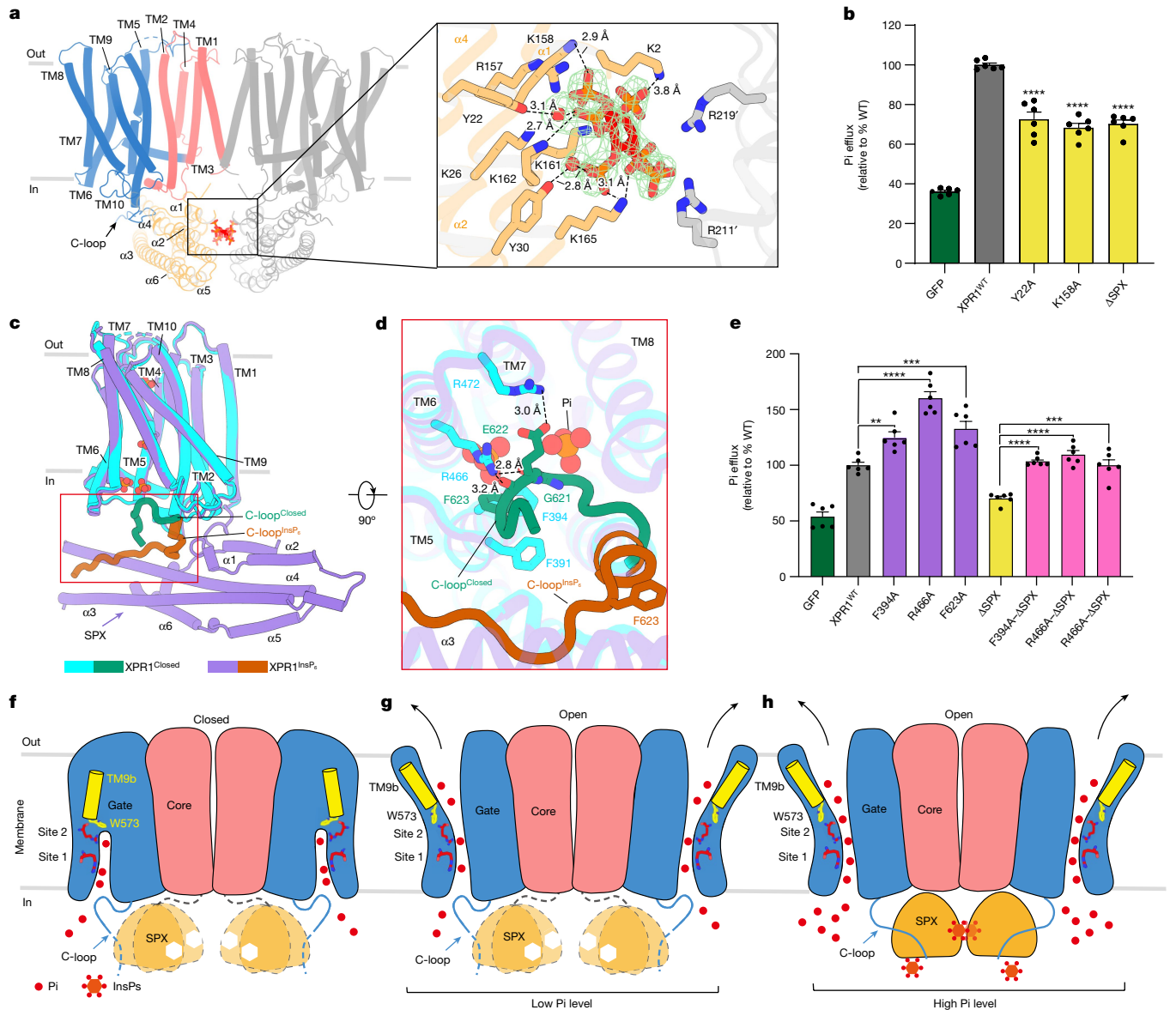


**Fig. 5 | InsP<sub>6</sub> regulation and a working model for Pi efflux by XPR1.** **a**, InsP<sub>6</sub>-binding site in the SPX domain. InsP<sub>6</sub> and interacting residues are shown in sticks. The red balls represent putative solvents. The density for InsP<sub>6</sub> and solvents are in green meshes. The black dashed lines represent polar interactions. **b**, Pi export activities of XPR1<sup>WT</sup> and variants with mutations in the InsP<sub>6</sub>-binding site. **c**, Superposition of XPR1<sup>Closed</sup> (cyan and green) and XPR1<sup>InsP<sub>6</sub></sup> (purple and orange). The red box indicates the focused area shown in panel **d**. **d**, Conformational changes between the C-loops of XPR1<sup>Closed</sup> (green) and XPR1<sup>InsP<sub>6</sub></sup> (orange). The residues involved in the interactions between the C-loop and the TMD are shown as side chains in sticks. The black dashed lines represent electrostatic interactions. **e**, Pi export activities of XPR1<sup>WT</sup> and variants with mutations in the

C-loop. **f–h**, Proposed working model for Pi efflux by XPR1. In the closed state, TM9 blocks the gate domain, and the C-loop binds to the TMD, which limits but not completely blocks Pi entry (**f**). When intracellular Pi levels are low, Pi could access the gate domain and trigger pore opening, resulting in a low degree of Pi export (**g**). When intracellular Pi levels are high, increased InsPPs bind to the SPX domain, which recruits the C-loop and releases it from the TMD, thereby facilitating the access of Pi to the gate domain and leading to a high degree of Pi efflux (**h**). For functional analyses in **b,e**, cells expressing GFP served as controls. Data were normalized to XPR1<sup>WT</sup> and are presented as mean  $\pm$  s.e.m.;  $n = 6$  from three independent replicates. One-way ANOVA was used: \*\* $P = 0.006$ , \*\*\* $P < 0.001$  and \*\*\*\* $P < 0.0001$ . Source Data are provided.

Figs. 7g–j and 9). In addition, the conserved R211 and R219 from the adjacent SPX domain appear to contribute to InsP<sub>6</sub> binding (Fig. 5a). The mutations Y22A and K158A reduced Pi export activities similar to that of XPR1<sup>ΔSPX</sup> (Fig. 5b), highlighting a crucial role of these residues in InsPP sensation. We further modelled the physiological relevant InsPP, 1,5-InsP<sub>8</sub>, into the InsP<sub>6</sub> site of XPR1 (Extended Data Fig. 10a–d). The fitted 1,5-InsP<sub>8</sub> has no clashes with the SPX domains and could establish proper interactions with the surrounding residues, most of which coincide with those with InsP<sub>6</sub> (Extended Data Fig. 10c,d). In particular, the 5-position diphosphate of 1,5-InsP<sub>8</sub> (or 5-InsP<sub>7</sub>) is positioned closer to Y22, K26 and K162 and could form stronger interactions

with these residues than InsP<sub>6</sub>. In addition, the 1-position diphosphate potentially forms interactions with R157, K158 and K161 (Extended Data Fig. 10c,d).

To reveal how the SPX domain regulates XPR1 activity, we aligned the structures of XPR1<sup>Closed</sup> and XPR1<sup>InsP<sub>6</sub></sup>, which showed dramatic conformational differences between the C-loops (Fig. 5c). Without adding InsP<sub>6</sub>, the SPX domain is invisible in XPR1<sup>Closed</sup>, presumably owing to conformational dynamics; furthermore, the hairpin-like C-loop is positioned at the bottom of Pi-binding site 1, which narrows the pathway for Pi accessing to site 1 (Fig. 5c and Extended Data Fig. 6f, green). Specifically, F623 on the C-loop of XPR1<sup>Closed</sup> stacks with F391 and F394 on

TM5, and R466 from TM6 forms electrostatic interactions with the backbone carbonyl oxygen atoms of G621 and E622 (Fig. 5d). By contrast, the C-loop of XPR1<sup>InsP<sub>6</sub></sup> shifts 15.8 Å (between Cα atoms of F623) away from site 1 and establishes extensive interactions with the SPX domain (Figs. 2f and 5d and Extended Data Fig. 6g, orange). On the basis of these structural observations, we hypothesized that the SPX domain regulates XPR1 activity by interacting with the C-loop. To substantiate this hypothesis, we assayed the Pi export activity of XPR1 variants with mutations that may affect the interactions between the intracellular Pi gate and the C-loop. Although the F394A, R466A and F623A mutants have slightly decreased cell-surface expression, they exhibit notably increased Pi export activity compared with XPR1<sup>WT</sup> (Fig. 5e and Supplementary Fig. 2a). Moreover, the same three mutations also increased the Pi export activity of XPR1<sup>ΔSPX</sup> to a similar level to that of XPR1<sup>WT</sup> (Fig. 5e). A previous study<sup>8</sup> has shown that several mutations in the C-loop of XPR1 caused impaired Pi export and pathological consequences.

## Discussion

On the basis of the structural and functional results, we propose a model for Pi transport and regulation by the SPX domain in XPR1 homologues (Fig. 5f–h). Pi is transported by the gate domain (previously known as the EXS domain) of the TMD; the positively charged sites 1 and 2 facilitate the recognition and binding of Pi to the gate domain. Elevated intracellular Pi levels increase its chemical gradient across the membrane, together with the resting membrane potential, which potentially serve as the driving force for the outwards movement of negatively charged Pi. The bound Pi in site 2 interacts with W573 and may trigger local conformational changes in TM9b, which opens the gate domain. Substitution of this W573 with an aromatic residue phenylalanine retained substantial Pi efflux activity, whereas the W573A mutation led to almost inactive XPR1 (Fig. 4f). Similarly, SLAC1 anion channels possess a conserved phenylalanine in the middle of the ion pathway, which is crucial for gating<sup>41</sup>. As the driving force is dissipating, W573 may reset its conformation and TM9b re-establishes interactions with TM6 and TM7, thereby closing the pore. This suggests that the gating mechanism is independent of the SPX domain, in line with the remaining Pi export activity of XPR1 and PHO1 without the SPX domain<sup>4,21</sup> (Fig. 1a,b). However, the SPX domain tunes the entry of Pi. Under low intracellular Pi levels, the SPX domain assumes dynamic conformations because of a low level of cytosolic InsPPs, and the C-loop folds into site 1 and restricts the entry of Pi, resulting in low Pi export activity (Fig. 5f,g). Increased intracellular Pi levels lead to the accumulation of InsPPs<sup>5</sup>, which can be sensed by the SPX domain and in turn liberate the C-loop from binding to site 1, thereby enhancing Pi efflux (Fig. 5h). Because the C-loop contributes to forming the vestibule of the Pi entry, more Pi fluxing in site 1 may stimulate the release of the C-loop and binding to the InsPP-bound SPX domain. Moreover, the Pi-binding sites, W573 in TM9, the key residues in the C-loop and the SPX domain are highly conserved in yeast SYG1, plant PHO1 and other XPR1 in metazoans; we therefore speculate that these XPR1 homologues should use a similar mechanism to maintain Pi homeostasis.

Most transporters alternatively open their extracellular or intracellular gates, but not simultaneously, during transporting diverse substances across the membrane, known as the alternating access mechanism<sup>42</sup>. CFTR (cystic fibrosis transmembrane conductance regulator) functions as a chloride channel despite assuming a classic ABC (ATP-binding cassette) transporter fold<sup>43,44</sup>, and glutamate transporter homologues exhibit chloride channel property uncoupled from transport<sup>45,46</sup>, suggesting a blurred boundary between transporters and channels<sup>47</sup>. In contrast to the canonical alternating-access mechanism, we demonstrated a hydrophilic conduit of more than 4 Å wide in the gate domain of XPR1<sup>open</sup> that connects the extracellular and intracellular sides, suggesting a channel-like mechanism for Pi export. In addition,

similar to the selectivity filter of ion channels, sites 1 and 2 of XPR1 have a role in Pi recognition and potential selectivity<sup>4</sup>. However, we hypothesize that XPR1 may not have a comparable flow rate to the tens of millions of ions per seconds of a typical channel (see the ‘Discussion’ section in Supplementary Information). Future investigation is required to determine the exact transport rate of XPR1. Nevertheless, the structures elucidate that XPR1 assumes a novel fold, distinguishing from known channels, but functions like a channel in exporting Pi.

Mutations in XPR1 have been reported to cause human PFBC<sup>6–8,39,48</sup>. We mapped these pathogenic mutations to our XPR1 structure, which demonstrates that 7 out of 14 of the reported mutations are concentrated in the SPX domain, 4 mutations are located in the gate domain, and the remaining 3 mutations reside in the C-loop (Extended Data Fig. 10e). Specifically, R459C and R570C, which contribute to forming Pi-binding sites 1 and 2, respectively, cause reduced Pi efflux and thus are associated with PFBC (Extended Data Fig. 10g). The pathogenic ΔL612–T696 mutant, which lacks the last two helical turns of TM10 and the entire C-loop (Extended Data Fig. 10h), not only eliminates the interactions between the C-loop and the intracellular site 1 but could also cause protein instability, reflected by its greatly decreased expression<sup>8</sup>. Moreover, N619D may enhance the interaction of the C-loop with the site 1 vestibule by engaging in stronger electrostatic interactions with R624 and the backbone nitrogen atoms of E622 and A625 than does N619, hindering the release of the C-loop; I629S may disrupt the hydrophobic interactions between the C-loop and the SPX domain (Extended Data Fig. 10h,i). Consistent with our structural observations, these structural elements have critical roles in Pi transport and regulation and thus are frequently targeted by pathogenic mutations that cause impaired Pi export. Similarly, mutations that cause plant phenotypes with reduced growth<sup>21,22,49,50</sup> are also enriched in the SPX domain and the gate domain of PHO1 (Extended Data Fig. 10f,j). In conclusion, the XPR1 structures represent an excellent example demonstrating the mode of action of how the SPX domain regulates Pi homeostasis by tuning the Pi export activity of a Pi transporter, and provide mechanistic insights into Pi binding and transport, InsPP recognition, and the coupling of Pi export and the SPX domain.

## Online content

Any methods, additional references, Nature Portfolio reporting summaries, source data, extended data, supplementary information, acknowledgements, peer review information; details of author contributions and competing interests; and statements of data and code availability are available at <https://doi.org/10.1038/s41586-024-07852-9>.

- Berndt, T. & Kumar, R. Phosphonins and the regulation of phosphate homeostasis. *Annu. Rev. Physiol.* **69**, 341–359 (2007).
- Goretti Penido, M. & Alon, U. S. Phosphate homeostasis and its role in bone health. *Pediatr. Nephrol.* **27**, 2039–2048 (2012).
- Austin, S. & Mayer, A. Phosphate homeostasis — a vital metabolic equilibrium maintained through the INPHORS signaling pathway. *Front. Microbiol.* **11**, 1367 (2020).
- Giovannini, D., Touhami, J., Charnet, P., Sitbon, M. & Battini, J. L. Inorganic phosphate export by the retrovirus receptor XPR1 in metazoans. *Cell Rep.* **3**, 1866–1873 (2013).
- Li, X. et al. Control of XPR1-dependent cellular phosphate efflux by InsP<sub>6</sub> is an exemplar for functionally-exclusive inositol pyrophosphate signaling. *Proc. Natl. Acad. Sci. USA* **117**, 3568–3574 (2020).
- Legati, A. et al. Mutations in XPR1 cause primary familial brain calcification associated with altered phosphate export. *Nat. Genet.* **47**, 579–581 (2015).
- Anheim, M. et al. XPR1 mutations are a rare cause of primary familial brain calcification. *J. Neurol.* **263**, 1559–1564 (2016).
- Lopez-Sanchez, U. et al. Characterization of XPR1/SLC53A1 variants located outside of the SPX domain in patients with primary familial brain calcification. *Sci. Rep.* **9**, 6776 (2019).
- Berndt, T. & Kumar, R. Novel mechanisms in the regulation of phosphorus homeostasis. *Physiology* **24**, 17–25 (2009).
- Murer, H., Hernando, N., Forster, I. & Biber, J. Proximal tubular phosphate reabsorption: molecular mechanisms. *Physiol. Rev.* **80**, 1373–1409 (2000).
- Hilfiker, H. et al. Characterization of a murine type II sodium-phosphate cotransporter expressed in mammalian small intestine. *Proc. Natl. Acad. Sci. USA* **95**, 14564–14569 (1998).
- Forster, I. C., Hernando, N., Biber, J. & Murer, H. Phosphate transporters of the SLC20 and SLC34 families. *Mol. Aspects Med.* **34**, 386–395 (2013).

13. Wege, S. & Poirier, Y. Expression of the mammalian xenotropic polytropic virus receptor 1 (XPR1) in tobacco leaves leads to phosphate export. *FEBS Lett.* **558**, 482–489 (2014).
14. Jennings, M. L. Role of transporters in regulating mammalian intracellular inorganic phosphate. *Front. Pharmacol.* **14**, 1163442 (2023).
15. Ansermet, C. et al. Renal Fanconi syndrome and hypophosphatemic rickets in the absence of xenotropic and polytropic retroviral receptor in the nephron. *J. Am. Soc. Nephrol.* **28**, 1073–1078 (2017).
16. Yao, X. P. et al. Analysis of gene expression and functional characterization of XPR1: a pathogenic gene for primary familial brain calcification. *Cell Tissue Res.* **370**, 267–273 (2017).
17. Poirier, Y., Thoma, S., Somerville, C. & Schiefelbein, J. Mutant of *Arabidopsis* deficient in xylem loading of phosphate. *Plant Physiol.* **97**, 1087–1093 (1991).
18. Hamburger, D., Rezzonico, E., MacDonald-Comber Petetot, J., Somerville, C. & Poirier, Y. Identification and characterization of the *Arabidopsis* PHO1 gene involved in phosphate loading to the xylem. *Plant Cell* **14**, 889–902 (2002).
19. Poirier, Y. & Bucher, M. Phosphate transport and homeostasis in *Arabidopsis*. *Arabidopsis Book* **1**, e0024 (2002).
20. Wang, Y., Ribot, C., Rezzonico, E. & Poirier, Y. Structure and expression profile of the *Arabidopsis* PHO1 gene family indicates a broad role in inorganic phosphate homeostasis. *Plant Physiol.* **135**, 400–411 (2004).
21. Wege, S. et al. The EXS domain of PHO1 participates in the response of shoots to phosphate deficiency via a root-to-shoot signal. *Plant Physiol.* **170**, 385–400 (2016).
22. Wild, R. et al. Control of eukaryotic phosphate homeostasis by inositol polyphosphate sensor domains. *Science* **352**, 986–990 (2016).
23. Secco, D. et al. The emerging importance of the SPX domain-containing proteins in phosphate homeostasis. *New Phytol.* **193**, 842–851 (2012).
24. Secco, D., Wang, C., Shou, H. & Whelan, J. Phosphate homeostasis in the yeast *Saccharomyces cerevisiae*, the key role of the SPX domain-containing proteins. *FEBS Lett.* **556**, 289–295 (2012).
25. Puga, M. I. et al. Novel signals in the regulation of Pi starvation responses in plants: facts and promises. *Curr. Opin. Plant Biol.* **39**, 40–49 (2017).
26. Jung, J. Y., Ried, M. K., Hothorn, M. & Poirier, Y. Control of plant phosphate homeostasis by inositol pyrophosphates and the SPX domain. *Curr. Opin. Biotechnol.* **49**, 156–162 (2018).
27. Guan, Z. et al. Mechanistic insights into the regulation of plant phosphate homeostasis by the rice SPX2-PHR2 complex. *Nat. Commun.* **13**, 1581 (2022).
28. Zhou, J. et al. Mechanism of phosphate sensing and signaling revealed by rice SPX1-PHR2 complex structure. *Nat. Commun.* **12**, 7040 (2021).
29. Guan, Z. et al. The cytoplasmic synthesis and coupled membrane translocation of eukaryotic polyphosphate by signal-activated VTC complex. *Nat. Commun.* **14**, 718 (2023).
30. Battini, J. L., Rasko, J. E. & Miller, A. D. A human cell-surface receptor for xenotropic and polytropic murine leukemia viruses: possible role in G protein-coupled signal transduction. *Proc. Natl Acad. Sci. USA* **96**, 1385–1390 (1999).
31. Tailor, C. S., Nouri, A., Lee, C. G., Kozak, C. & Kabat, D. Cloning and characterization of a cell surface receptor for xenotropic and polytropic murine leukemia viruses. *Proc. Natl Acad. Sci. USA* **96**, 927–932 (1999).
32. Yang, Y. L. et al. Receptors for polytropic and xenotropic mouse leukaemia viruses encoded by a single gene at Rmc1. *Nat. Genet.* **21**, 216–219 (1999).
33. Tsai, J. Y. et al. Structure of the sodium-dependent phosphate transporter reveals insights into human solute carrier SLC20. *Sci. Adv.* **6**, eabb4024 (2020).
34. Dong, Y. et al. Structure and mechanism of the human NHE1-CHP1 complex. *Nat. Commun.* **12**, 3474 (2021).
35. Arakawa, T. et al. Crystal structure of the anion exchanger domain of human erythrocyte band 3. *Science* **350**, 680–684 (2015).
36. Jumper, J. et al. Highly accurate protein structure prediction with AlphaFold. *Nature* **596**, 583–589 (2021).
37. Parker, J. L., Corey, R. A., Stansfeld, P. J. & Newstead, S. Structural basis for substrate specificity and regulation of nucleotide sugar transporters in the lipid bilayer. *Nat. Commun.* **10**, 4657 (2019).
38. Capper, M. J. et al. Substrate binding and inhibition of the anion exchanger 1 transporter. *Nat. Struct. Mol. Biol.* **30**, 1495–1504 (2023).
39. Guo, X. X. et al. Spectrum of SLC20A2, PDGFRB, PDGFB, and XPR1 mutations in a large cohort of patients with primary familial brain calcification. *Hum. Mutat.* **40**, 392–403 (2019).
40. Drew, D. & Boudker, O. Shared molecular mechanisms of membrane transporters. *Annu. Rev. Biochem.* **85**, 543–572 (2016).
41. Chen, Y. H. et al. Homologous structure of the SLAC1 anion channel for closing stomata in leaves. *Nature* **467**, 1074–1080 (2010).
42. Drew, D., North, R. A., Nagarathinam, K. & Tanabe, M. Structures and general transport mechanisms by the major facilitator superfamily (MFS). *Chem. Rev.* **121**, 5289–5335 (2021).
43. Gadsby, D. C., Vergani, P. & Csanady, L. The ABC protein turned chloride channel whose failure causes cystic fibrosis. *Nature* **440**, 477–483 (2006).
44. Levring, J. et al. CFTR function, pathology and pharmacology at single-molecule resolution. *Nature* **616**, 606–614 (2023).
45. Fairman, W. A., Vandenberg, R. J., Arriza, J. L., Kavanaugh, M. P. & Amara, S. G. An excitatory amino-acid transporter with properties of a ligand-gated chloride channel. *Nature* **375**, 599–603 (1995).
46. Chen, I. et al. Glutamate transporters have a chloride channel with two hydrophobic gates. *Nature* **591**, 327–331 (2021).
47. Gadsby, D. C. Ion channels versus ion pumps: the principal difference, in principle. *Nat. Rev. Mol. Cell Biol.* **10**, 344–352 (2009).
48. Ramos, E. M. et al. Primary brain calcification: an international study reporting novel variants and associated phenotypes. *Eur. J. Hum. Genet.* **26**, 1462–1477 (2018).
49. Liu, T. Y. et al. PHO2-dependent degradation of PHO1 modulates phosphate homeostasis in *Arabidopsis*. *Plant Cell* **24**, 2168–2183 (2012).
50. Vetal, P. V. & Poirier, Y. The *Arabidopsis* PHOSPHATE 1 exporter undergoes constitutive internalization via clathrin-mediated endocytosis. *Plant J.* <https://doi.org/10.1111/tpj.16441> (2023).

**Publisher's note** Springer Nature remains neutral with regard to jurisdictional claims in published maps and institutional affiliations.

Springer Nature or its licensor (e.g. a society or other partner) holds exclusive rights to this article under a publishing agreement with the author(s) or other rightsholder(s); author self-archiving of the accepted manuscript version of this article is solely governed by the terms of such publishing agreement and applicable law.

© The Author(s), under exclusive licence to Springer Nature Limited 2024

## Methods

### Pi export assay

The Pi export assay was performed as previously described<sup>16</sup> with modifications. HEK293T (Gibco) cells were seeded on 12-well plates at  $2 \times 10^5$  cells per well in DMEM (Gibco) with 10% FBS (PAN-Biotech). The seeded cells were cultured at 37 °C with 5% CO<sub>2</sub> on day 1. Cells in each well were transfected with 1 µg plasmids of XPR1<sup>WT</sup>, mutants or GFP mixed with 2 µl Lipofectamine 2000 (Invitrogen) on day 2. The Pi export assay was performed on day 3. Cells were washed three times with phosphate-free DMEM (Gibco) and incubated in phosphate-free DMEM for 1 h at 37 °C. Then, the supernatant was collected and Pi levels in the supernatant were measured with the Malachite Green Phosphate Assay Kit MAK307 (Sigma). Cells were lysed with 500 µl RIPA lysis buffer (50 mM Tris, pH 7.4, 150 mM NaCl, 1% Triton X-100, 1% sodium deoxycholate, 0.1% SDS, sodium orthovanadate, sodium fluoride, EDTA and leupeptin; Beyotime) at room temperature for 10 min and the lysates were transferred to 96-well plates to determine the total protein concentration using a BCA protein assay kit (Beyotime). The transport activities were normalized to the total protein concentration. For the time course of Pi export, export reactions were stopped at time-lines of 15, 30, 60, 90, 120 and 150 min, and Pi levels were measured as described above. All measurements were repeated at least three times on different days; for each measurement on the same day, Pi efflux assays were performed using cells from two or three different wells independently. To validate plasma membrane localization, HEK293T cells expressing GFP alone, GFP-tagged XPR1<sup>WT</sup> and all the mutants were imaged by the A1R Si laser scanning confocal microscope (CLSM) for GFP fluorescence (488 nm) and brightfield. The confocal images are presented in Supplementary Fig. 1.

### Cell-surface biotinylation assay

HEK293T cells were seeded on 100-mm dishes and were transfected with 20 µg plasmids of XPR1 variants (fused with a GFP at the C terminus) when cells at 70% confluence using polyethylenimine 25K (PEI 25K; Polysciences) at a ratio of 1:3 (w/w). Sixty hours later, cells were washed three times with ice-cold PBS (pH 8.0) and were incubated with 1 mg ml<sup>-1</sup> EZ-Link NHS-SS-biotin (A8005, APExBIO) in 3 ml PBS at room temperature for 30 min. Then, cells were incubated in 3 ml PBS supplemented with 50 mM Tris at room temperature for 20 min to remove the excessive EZ-Link NHS-SS-biotin. Subsequently, cells were washed three times with ice-cold PBS. Washed cells were collected and lysed for 10 min on ice using 3 ml RIPA lysis buffer (Beyotime) containing protease inhibitors. The cell lysates were centrifuged at 16,200g for 15 min. The supernatants were incubated with prewashed NeutrAvidin Agarose Resin beads (Thermo Fisher Scientific) for 1 h at 4 °C. Beads were then washed with RIPA lysis buffer to remove non-biotinylated proteins. The biotinylated cell-surface proteins were eluted from the beads using RIPA lysis buffer containing 50 mM dithiothreitol and protease inhibitors at room temperature for 2 h. The eluted samples were assayed by western blot analysis and in-gel fluorescence imaging.

### Western blot analysis

To probe the cell-surface expression levels of biotinylated XPR1 and mutants, the eluted samples from biotinylation assay were normalized to the total protein concentrations of cell lysates measured using a BCA protein assay kit (Beyotime). The normalized samples were assayed using SDS-PAGE. The gels were imaged by in-gel fluorescence excited at 488 nm using a Tanon 5200 Multi imager, and then were transferred onto nitrocellulose membranes (Bio-Rad). The transferred membranes were blocked in TBST buffer (20 mM Tris-HCl (pH 7.5), 150 mM NaCl and 0.1% w/v Tween-20) supplemented with 7% w/v non-fat dry milk at room temperature for 1 h. After washing three times with TBST, primary antibody of anti-GFP or the anti-Na<sup>+</sup>/K<sup>+</sup> pump (Proteintech) was added at a dilution of 1:5,000 and incubated at 4 °C overnight. Subsequently, the

membranes were washed three times with TBST and were added with anti-rabbit secondary antibody (Proteintech) at a dilution of 1:5,000 at room temperature for 1 h. Following washing three times with TBST, blots were performed using BeyoECL plus (Beyotime) and visualized using a ChemiDoc MP imaging system (Bio-Rad). The western blot and the in-gel fluorescence results are presented in Supplementary Fig. 2.

### Expression and purification of XPR1

The gene of full-length human XPR1<sup>WT</sup> (UniProt accession code: Q9UBH6) was cloned and inserted into a pEG2 vector with an HRV 3C protease site, GFP and a Twin-Strep tag at the C terminus. All XPR1 mutants were generated by standard site-directed mutagenesis methods using a Mut Express II Fast Mutagenesis Kit (Vazyme Biotech). All plasmids were confirmed by DNA sequencing. The plasmids were transformed into DH10Bac-competent cells (Thermo Fisher) to generate bacmids. Then, the baculoviruses were produced in *Spodoptera frugiperda* Sf9 insect cells using the Bac-to-Bac baculovirus expression system (Invitrogen). P2 viruses were collected and used for protein expression. HEK293F (Gibco) cells were cultured in OPM-293 medium (OPM), shaking at 125 rpm min<sup>-1</sup> in a 37 °C incubator with 5% CO<sub>2</sub>. When cell density reached approximately  $2.5 \times 10^6$  cells per millilitre (C100, RWD), P2 baculoviruses were added to the medium at a ratio of 1:100 (v/v). After 12 h of culturing, 10 mM sodium butyrate (Sigma) was added to the medium to boost protein expression. After an additional 48 h, the cells were harvested by centrifugation at 1,700g for 3 min and the cell pellets were stored in a -80 °C freezer.

For purification of XPR1 and XPR1<sup>ASPx</sup>, cell pellets were resuspended in buffer A containing 20 mM HEPES (pH 7.5), 150 mM NaCl, 2 mM β-mercaptoethanol (β-ME) and a protease inhibitor cocktail including 1 mM phenylmethylsulfonic acid acyl fluoride, 0.8 µM pepstatin, 2 µM leupeptin and 2 µM aprotinin. Resuspended cells were manually homogenized by using a glass Dounce homogenizer on ice. Membrane fractions were collected by ultracentrifugation at 158,600g for 30 min and solubilized in buffer A supplemented with 1% (w/v) n-dodecyl-β-D-maltoside (Anatrace) and 0.15% (w/v) cholesterol hemisuccinate (Anatrace) for 1.5 h at 4 °C. After another ultracentrifugation at 158,600g for 30 min, the supernatant was incubated with Streptactin beads (Smart-Lifesciences) for 1 h at 4 °C. The resin was washed with 10 column volumes of wash buffer (20 mM HEPES (pH 7.5), 150 mM NaCl, 2 mM β-ME and 0.06% (w/v) GDN). Then, the protein was eluted with wash buffer supplemented with 5 mM desthiobiotin (Sigma). The GFP and Twin-strep tag was cleaved by PreScission protease (1:25 w/w ratio) on ice for 2 h. Subsequently, the tag-removed protein was concentrated and subjected onto a Superose 6 increase 10/300 GL column (Cytiva) equilibrated with buffer containing 25 mM NaH<sub>2</sub>PO<sub>4</sub> (pH 7.5), 150 mM NaCl, 2 mM β-ME and 0.0075% (w/v) GDN. The peak fractions were concentrated to 17.5 mg ml<sup>-1</sup> for cryo-EM grid preparation or for SEC coupled with multi-angle static light scattering (SEC-MALS) analysis.

For purification of the XPR1-InsP<sub>6</sub> complex, InsP<sub>6</sub> (Sigma) was added to the purification buffers and to the gel-filtration buffer at a concentration of 1 mM. Peak fractions from gel filtration were concentrated to 16.0 mg ml<sup>-1</sup> for cryo-EM grid preparation.

### SEC-MALS analysis

SEC-MALS analysis was conducted using an AKTA Pure protein purification system (Cytiva) equipped with a miniDAWN TREOS light scattering detector and a refractometer Optilab T-rEX (Wyatt Technology). The purified samples of XPR1 and XPR1<sup>ASPx</sup> were diluted to a concentration of 1 mg ml<sup>-1</sup>. Of each diluted sample, 100 µl was injected onto a Superose 6 increase 10/300 GL column (Cytiva) equilibrated with buffer containing 25 mM NaH<sub>2</sub>PO<sub>4</sub> (pH 7.5), 150 mM NaCl, 2 mM β-ME, 0.05% (w/v) Na<sub>3</sub> and 0.0075% (w/v) GDN with a flow rate of 0.3 ml min<sup>-1</sup>. The molecular masses of the corresponding peaks were determined by the ASTRA6.1 software (Wyatt Technology). A dn/dc (the refractive index increment) value of 0.185 and an extinction coefficient (1 mg ml<sup>-1</sup>) of

1.45 for protein were used. Because the  $d\text{n}/d\text{c}$  value for detergent GDN is unknown, an arbitrary value of  $0.143 \text{ ml g}^{-1}$  from a previous study<sup>51</sup> was applied. Although this arbitrary value for GDN was used, it did not affect the calculation of the molecular mass of the membrane proteins.

### Cryo-EM sample preparation and data collection

The purified samples were centrifuged at  $15,600\text{g}$  (M1324R, RWD) for 20 min at  $4^\circ\text{C}$  before cryo-EM sample preparation. Aliquots of  $3.0 \mu\text{l}$  samples were added to glow-discharged grids (Quantifoil, 300 mesh, R1.2/1.3, Au). The grids were blotted for 3.0–4.5 s at  $4^\circ\text{C}$  with 100% humidity, and plunged into liquid ethane and cooled by liquid nitrogen using a Vitrobot Mark IV (Thermo Fisher Scientific).

All datasets were collected using a 300 kV Titan Krios microscope (Thermo Fisher Scientific) equipped with a K3 direct electron detector and a GIF quantum energy filter (Gatan). All movie stacks were automatically acquired using EPU v3 (Thermo Fisher Scientific) at a nominal magnification of 105,000 with a pixel size of  $0.85 \text{ \AA}$ . The dose rate was adjusted to 15 counts per pixel per second. All movie stacks were fractionated into 32 frames with an exposure time of 2.69 s. The defocus range was set between  $-1.0$  and  $-2.0 \mu\text{m}$ .

### Cryo-EM data processing

All movie stacks were imported into RELION-3 (ref. 52) and were motion-corrected, binned by twofold and dose-weighted using MotionCorr2 (ref. 53) with  $5 \times 5$  patches. The defocus values of each summed micrograph were estimated using Gctf<sup>54</sup>. Particles were initially picked from roughly 200 micrographs using the LoG-based auto-picking in RELION-3. These particles were subjected to two rounds of 2D classification to generate templates for subsequent template-based particle picking. A total of 636,011 particles were picked and extracted in a box of 320 pixels. Then, the particles were imported into CryoSPARC<sup>55</sup> and subjected to one round of 2D classification to remove junk particles, resulting in 391,369 good particles. Subsequently, ab initio reconstruction was conducted to generate an initial map. Multi-reference 3D classification with  $C_2$  symmetry imposed was performed, resulting in a major class of 66% of total particles with clearly resolved transmembrane helices. Particles from this class were selected and subjected to non-uniform refinement with  $C_2$  symmetry imposed, yielding a refined map at  $3.01 \text{ \AA}$  resolution. Further local refinement with  $C_2$  symmetry imposed with a mask covering only the transmembrane domain yielded an improved map at  $2.96 \text{ \AA}$  resolution. The particles were imported back to RELION-3 and were polished. Next, the polished particles were subjected to 2D classification in CryoSPARC. Finally, a  $2.84 \text{ \AA}$  resolution map of XPR1 was obtained after non-uniform and local refinements.

To better identify the state of heterogeneity of the particles, we performed symmetry expansion in RELION-3 using the polished particles. The particles were doubled to 516,972 and were subjected to skip-alignment 3D classification ( $T = 30; K = 6$ ) with a mask focused on one monomer. The two classes showed obvious conformational differences compared with the other four classes, accounting for up to 15% of the total particles for this 3D classification. After two rounds of 3D classification using a soft mask covering a monomer of XPR1 in CryoSPARC, a class of 40,195 particles was subjected to further local refinement without imposing symmetry. The resulting map of XPR1 in an open state was obtained at a resolution of  $3.61 \text{ \AA}$ . A detailed flowchart of cryo-EM data processing is presented in Extended Data Figs. 2 and 3.

The XPR1<sup>InsP<sub>6</sub></sup> data were processed similarly. In brief, a total of 1,909,405 picked particles were extracted with a binning factor of 2. The particles were imported into CryoSPARC and subjected to two rounds of 2D classification to remove junk particles, resulting in 839,824 good particles. Subsequently, ab initio reconstruction was conducted to generate an initial map. After one round of multi-reference 3D classification with  $C_2$  symmetry imposed, the reconstruction map from

the major class (61% of total particles) clearly showed electron microscopy densities for the TMD and the SPX domain. The 510,733 particles were imported back to RELION-3.1 and were subjected to local 3D classification ( $T = 8; K = 6$ ) without imposing symmetry. One class showing a clearly resolved SPX domain was selected for further refinement. After polishing, the 108,829 particles were subjected to skip-alignment 3D classification ( $T = 30; K = 4$ ) with a mask covering the TMD and the SPX domain. Two classes showing different conformations in the C-loop region were subjected to further local refinement with  $C_2$  symmetry imposed in CryoSPARC. The final map of XPR1<sup>InsP<sub>6</sub></sup> from 30,798 particles was obtained at a resolution of  $2.96 \text{ \AA}$ . The other map with weak density for the SPX domain from 40,414 particles was refined to a resolution of  $3.13 \text{ \AA}$ . A detailed flowchart of cryo-EM data processing is presented in Extended Data Fig. 4.

### Model building and refinement

The predicted AlphaFold2 model of XPR1 was fitted into the cryo-EM density map of XPR1 in Chimera<sup>56</sup> and was manually inspected and adjusted in Coot<sup>57</sup>. Refinement of the XPR1 model against the cryo-EM map in real space was performed using the phenix.real\_space\_refine in PHENIX<sup>58</sup>. After model refinement, cholesterol, phosphatidylcholine lipid, Pi and water molecules were manually fitted into the extra densities within the maps. The models were further refined in PHENIX. The model versus map Fourier shell correlation curve was calculated by Phenix.mtrage. For XPR1<sup>Open</sup> and XPR1<sup>InsP<sub>6</sub></sup>, the XPR1<sup>Closed</sup> structure was manually fitted into the electron microscopy maps of XPR1<sup>Open</sup> and XPR1<sup>InsP<sub>6</sub></sup> in Chimera, respectively. Next, the models were checked and corrected in Coot. The resulting models were refined in Phenix as described above. The statistics of cryo-EM data collection and model refinement are summarized in Supplementary Table 1.

All figures were prepared with ChimeraX<sup>59</sup> and PyMol (Schrödinger, LLC).

### Reporting summary

Further information on research design is available in the Nature Portfolio Reporting Summary linked to this article.

### Data availability

The UniProt accession codes are Q9UBH6 (*Homo sapiens* XPR1), Q8S403 (*A. thaliana* PHO1) and P40528 (*S. cerevisiae* SYG1). The Protein Data Bank coordinates used for structural alignments are 5IJH (SPX of human XPR1), 5IJJ (SPX of *Chaetomium thermophilum* Gde1), 5JP (SPX of *Chaetomium thermophilum* Vtc4) and 5IIG (SPX of *S. cerevisiae* Vtc4). The 3D cryo-EM density maps of human XPR1<sup>Open</sup>, XPR1<sup>Closed</sup> and XPR1<sup>InsP<sub>6</sub></sup> have been deposited to the Electron Microscopy Data Bank under the accession numbers EMD-38067, EMD-38065 and EMD-38065, respectively. The coordinates of human XPR1<sup>Open</sup>, XPR1<sup>Closed</sup> and XPR1<sup>InsP<sub>6</sub></sup> have been deposited to the Protein Data Bank under the accession codes 8XSE, 8XSB and 8XF, respectively. Source data are provided with this paper.

51. Rouge, L. et al. Structure of CD20 in complex with the therapeutic monoclonal antibody rituximab. *Science* **367**, 1224–1230 (2020).
52. Zivanov, J. et al. New tools for automated high-resolution cryo-EM structure determination in RELION-3. *eLife* **7**, e42166 (2018).
53. Zheng, S. Q. et al. MotionCor2: anisotropic correction of beam-induced motion for improved cryo-electron microscopy. *Nat. Methods* **14**, 331–332 (2017).
54. Zhang, K. Gctf: real-time CTF determination and correction. *J. Struct. Biol.* **193**, 1–12 (2016).
55. Punjani, A., Rubinstein, J. L., Fleet, D. J. & Brubaker, M. A. cryoSPARC: algorithms for rapid unsupervised cryo-EM structure determination. *Nat. Methods* **14**, 290–296 (2017).
56. Pettersen, E. F. et al. UCSF Chimera – a visualization system for exploratory research and analysis. *J. Comput. Chem.* **25**, 1605–1612 (2004).
57. Emsley, P. & Cowtan, K. Coot: model-building tools for molecular graphics. *Acta Crystallogr. D Biol. Crystallogr.* **60**, 2126–2132 (2004).
58. Afonine, P. V. et al. Real-space refinement in PHENIX for cryo-EM and crystallography. *Acta Crystallogr. D Struct. Biol.* **74**, 531–544 (2018).
59. Pettersen, E. F. et al. UCSF ChimeraX: structure visualization for researchers, educators, and developers. *Protein Sci.* **30**, 70–82 (2021).

# Article

**Acknowledgements** We thank B. Xu at the Cryo-EM Center of the School of Advanced Agricultural Sciences of Peking University for support in cryo-EM data collection; D. Sun at the Cryo-EM Facility at the Institute of Physics, Chinese Academy of Science and Beijing Branch of Songshan Lake Materials Laboratory for support in cryo-EM sample preparation; and W. Fan for research assistance. This work is funded by the National Natural Science Foundation of China (T2221001 and 32271272 to D.J., U23A20143 and 32070031 to J.J.), and the Institute of Physics, Chinese Academy of Sciences (E0VK101 and E2V4101 to D.J.).

**Author contributions** D.J. conceived and designed the experiments. R.Y., H.C. and C.L. prepared the samples for the cryo-EM study and made all the constructs. D.W., H.C. and J.Z. collected cryo-EM data. H.C. and R.Y. processed the data, and built and refined the models. C.L. and R.Y. performed the Pi export assay. R.Y., H.C. and C.L. performed the western blot assay, confocal imaging and SEC-MALS analysis. R.Y. and H.C. prepared the figures. R.Y., H.C., C.L., J.J., J.G.

and D.J. analysed and interpreted the results. D.J. wrote the paper. All authors reviewed and revised the paper.

**Competing interests** The authors declare no competing interests.

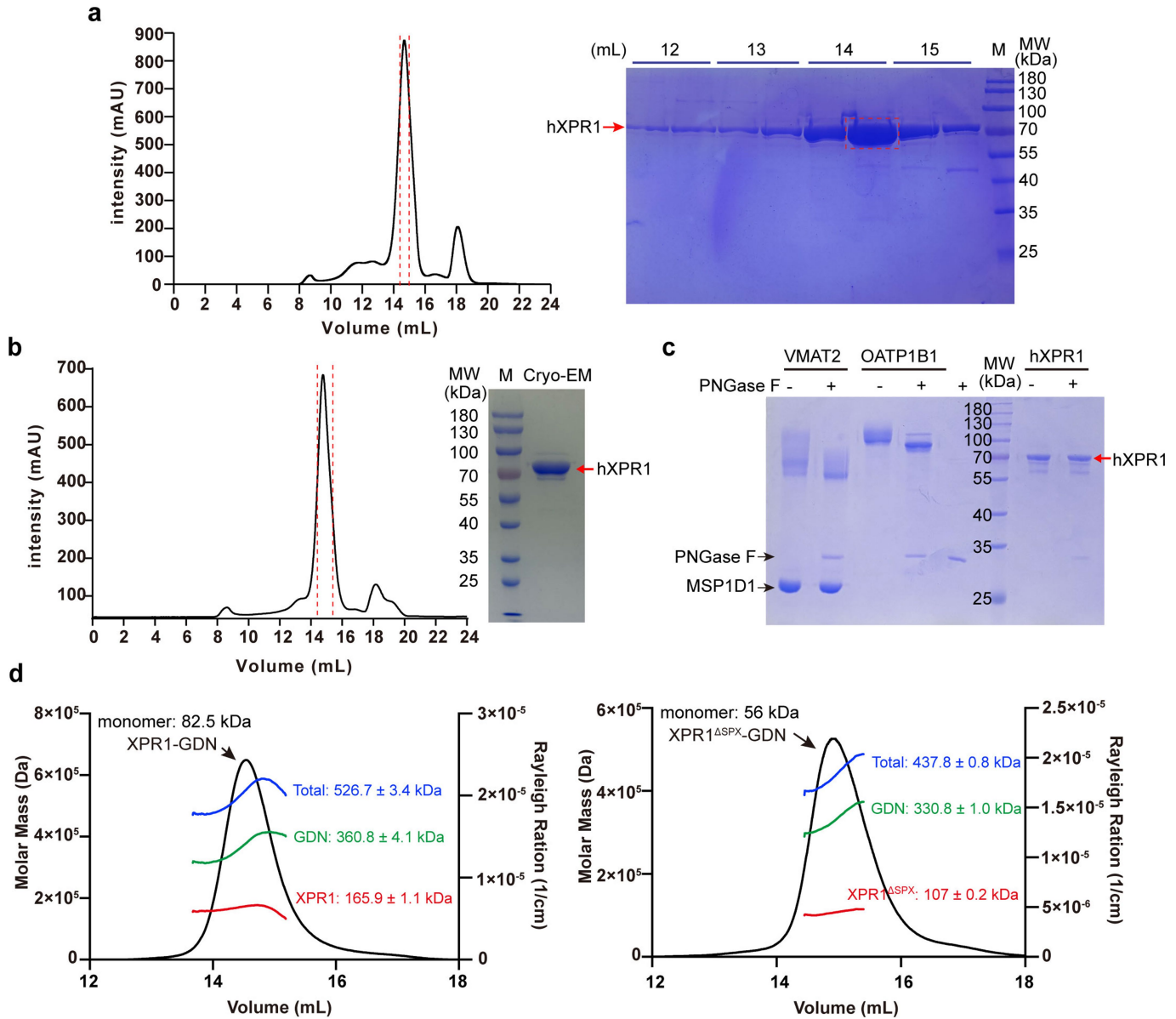
## Additional information

**Supplementary information** The online version contains supplementary material available at <https://doi.org/10.1038/s41586-024-07852-9>.

**Correspondence and requests for materials** should be addressed to Daohua Jiang.

**Peer review information** *Nature* thanks Kenji Inaba and the other, anonymous, reviewer(s) for their contribution to the peer review of this work. Peer reviewer reports are available.

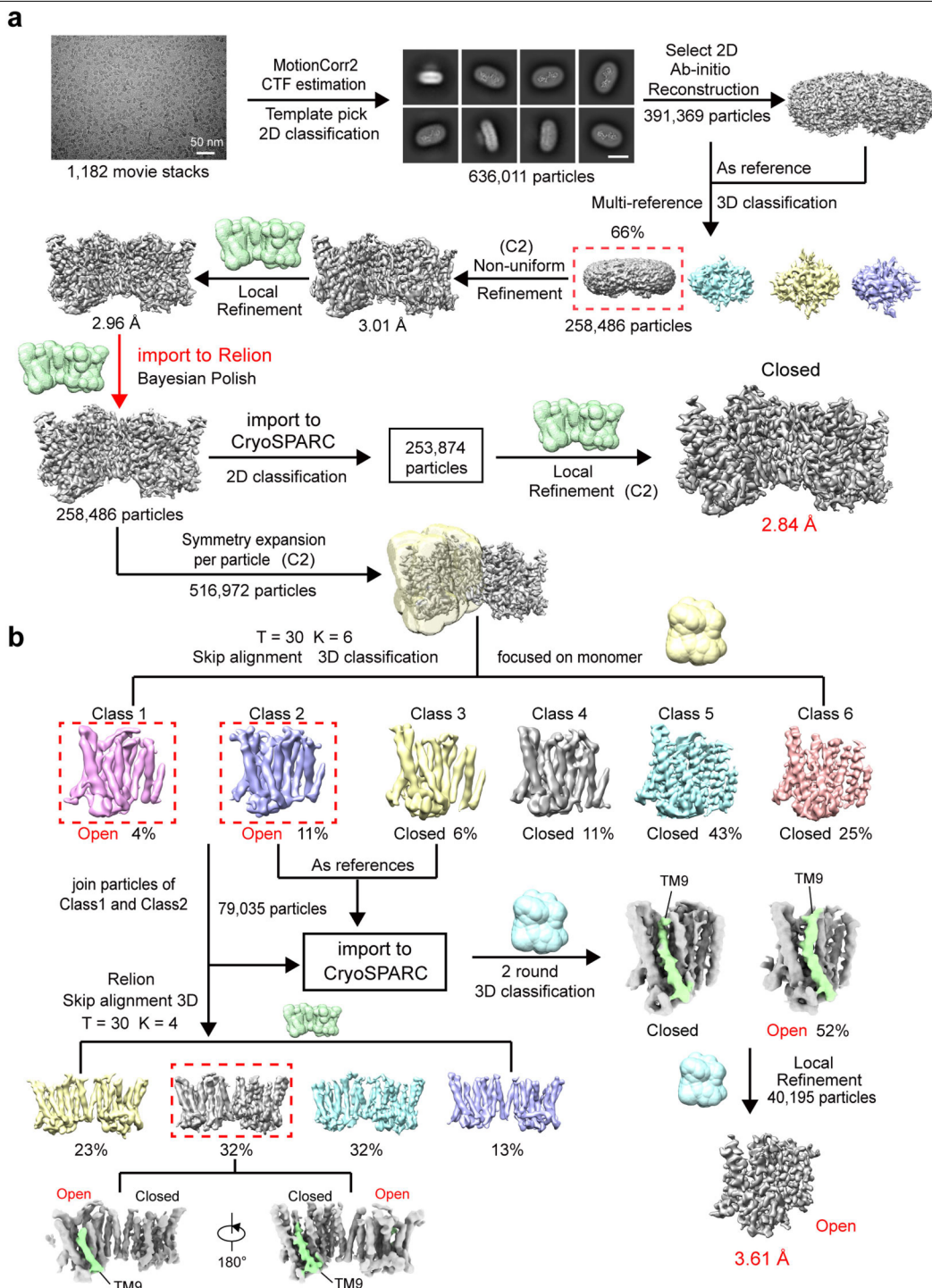
**Reprints and permissions information** is available at <http://www.nature.com/reprints>.



**Extended Data Fig. 1 | Purification of human XPR1.** **a,b**, A representative size-exclusion chromatography (SEC) profile of purified human XPR1 samples without (**a**) or with (**b**) 1 mM InsP6. Peak fractions used for cryo-EM analysis are indicated by red dashed lines. Peak fractions from SEC were visualized by SDS-PAGE with Coomassie blue staining. Red arrow indicates the bands of hXPR1. Red dashed box indicates XPR1 samples used for cryo-EM analysis. The purification of XPR1 with or without InsP6 were repeated at least three times independently with similar results. **c**, Digestion of the purified XPR1 (in detergents) by PNGase F. VMAT2 (in nanodiscs) and OATP1B1 (in detergents) serve as controls. PNGase F was added to the respective samples at a ratio of

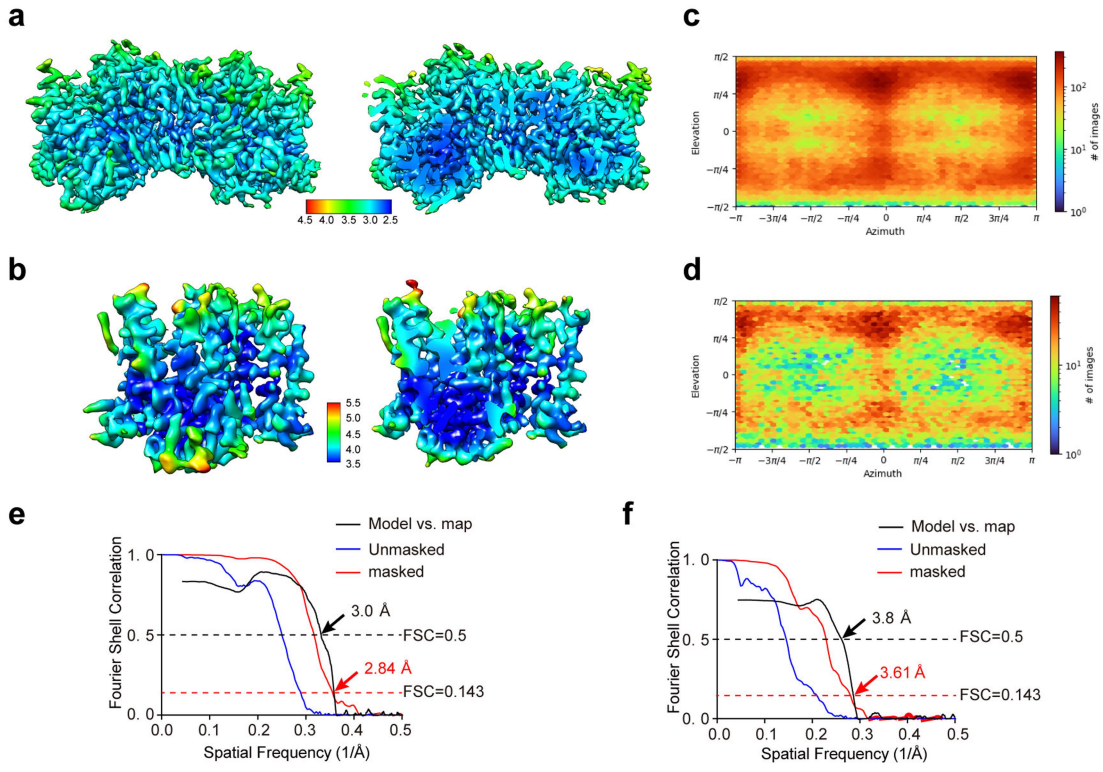
1:10 (w/w). The mixtures were incubated at 37 °C for 3 h and were visualized by SDS-PAGE stained by Coomassie blue. The PNGase F digestion experiments were repeated three times independently with similar results. **d**, SEC-MALS analyses of purified XPR1 $^{\text{WT}}$  (left) and XPR1 $^{\Delta\text{ASPX}}$  (right). The light scattering trace for XPR1 is shown as a black line. The molar masses of the protein–detergent complex (Total, blue), the detergent micelle (GDN, green) and the protein (XPR1 or XPR1 $^{\Delta\text{ASPX}}$ , red) are indicated. The same Superose 6 increase 10/300 GL column was used for the XPR1 purification and SEC-MALS analysis. Source Data are provided.

# Article



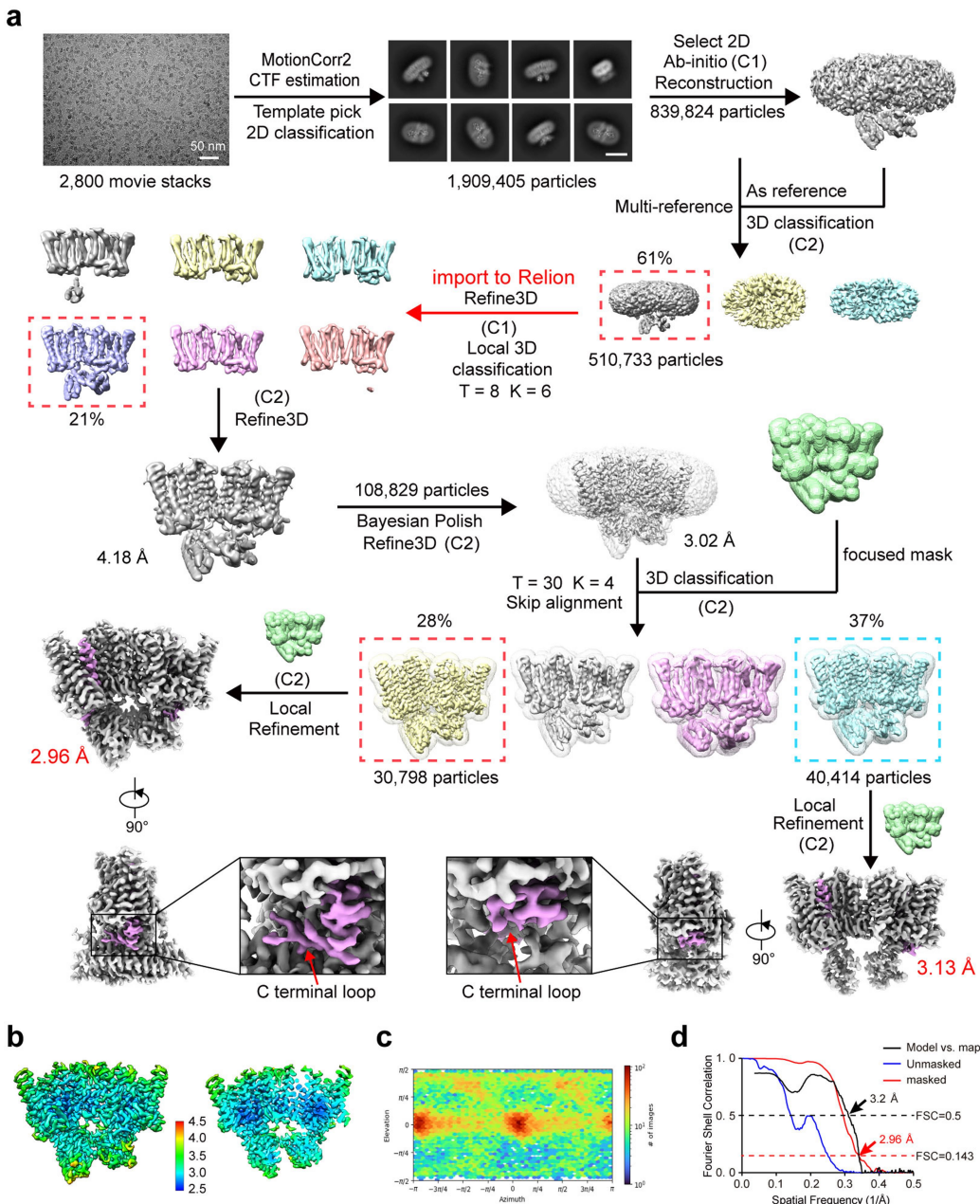
**Extended Data Fig. 2 | Cryo-EM data processing of human XPRI.** **a**, The flowchart for cryo-EM data processing of XPRI<sup>Closed</sup>. A representative motion-corrected electron micrograph (out of 1,182 micrographs) of XPRI. Scale bar, 50 nm. Scale bar in reference-free 2D class averages is 10 nm. **b**, The flowchart

for cryo-EM data processing of XPRI<sup>Open</sup>. The red dashed boxes indicate 3D classes in open conformation from the focused skip-alignment 3D classification. These selected particles were imported into CryoSPARC to generate the final map of XPRI<sup>Open</sup>.



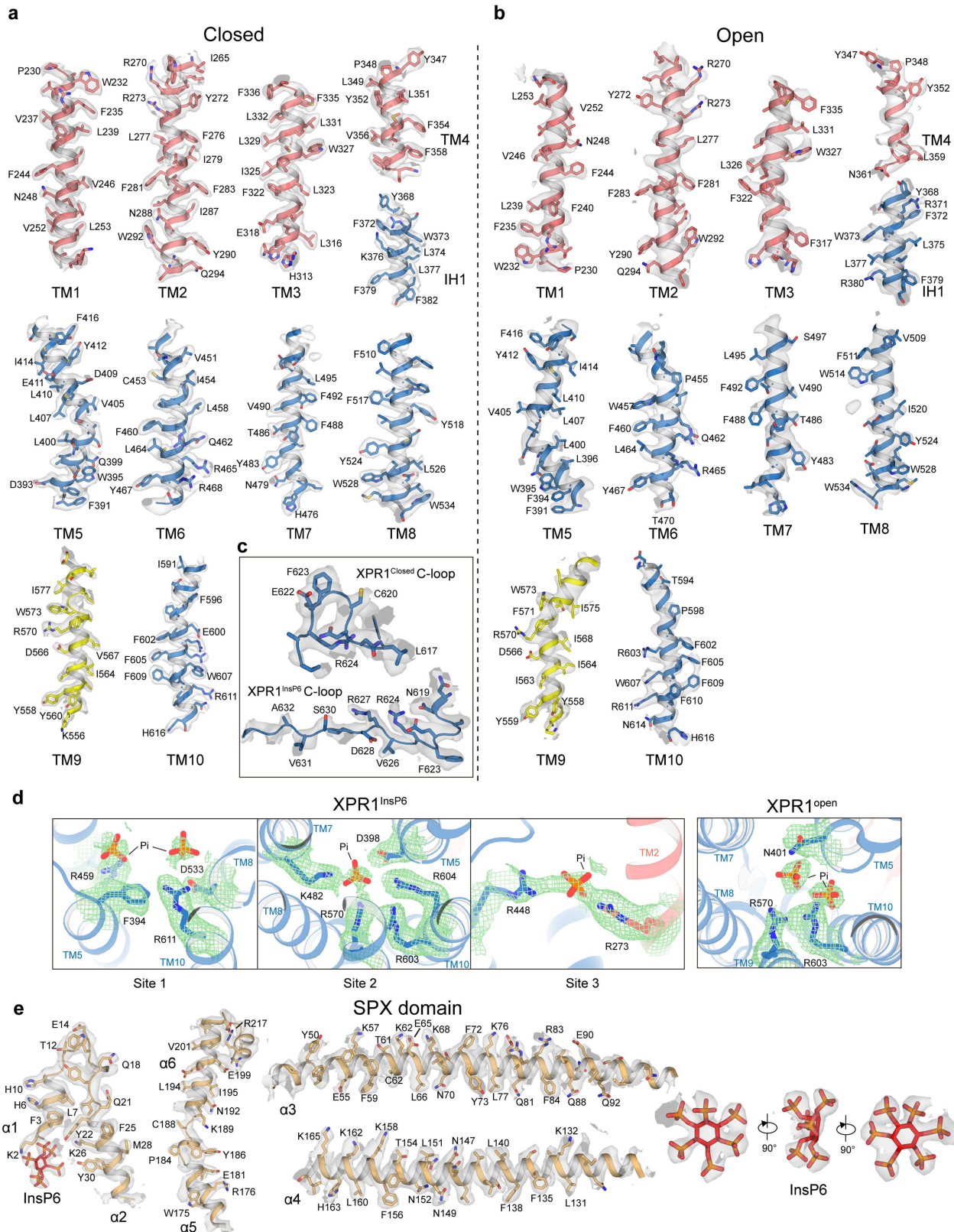
**Extended Data Fig. 3 | Cryo-EM analysis of XPR1<sup>Closed</sup> and XPR1<sup>Open</sup>.** **a,b**, Local resolution distribution maps of XPR1<sup>Closed</sup> (**a**) and XPR1<sup>Open</sup> (**b**). **c,d**, Particle angular distribution calculated in CryoSPARC for the final reconstruction of XPR1<sup>Closed</sup> (**c**) and XPR1<sup>Open</sup> (**d**). **e,f**, Fourier-shell correlation (FSC) analysis of XPR1<sup>Closed</sup> (**e**) and XPR1<sup>Open</sup> (**f**). The FSC curves of the final EM map without and

with a solvent mask are colored in blue and red, respectively. Red arrows indicate the resolution of the map when FSC = 0.143. The FSC curve of the refined model fitting in the final EM map is colored in black. Black arrows indicate the resolution of model-map fitting when FSC = 0.5.



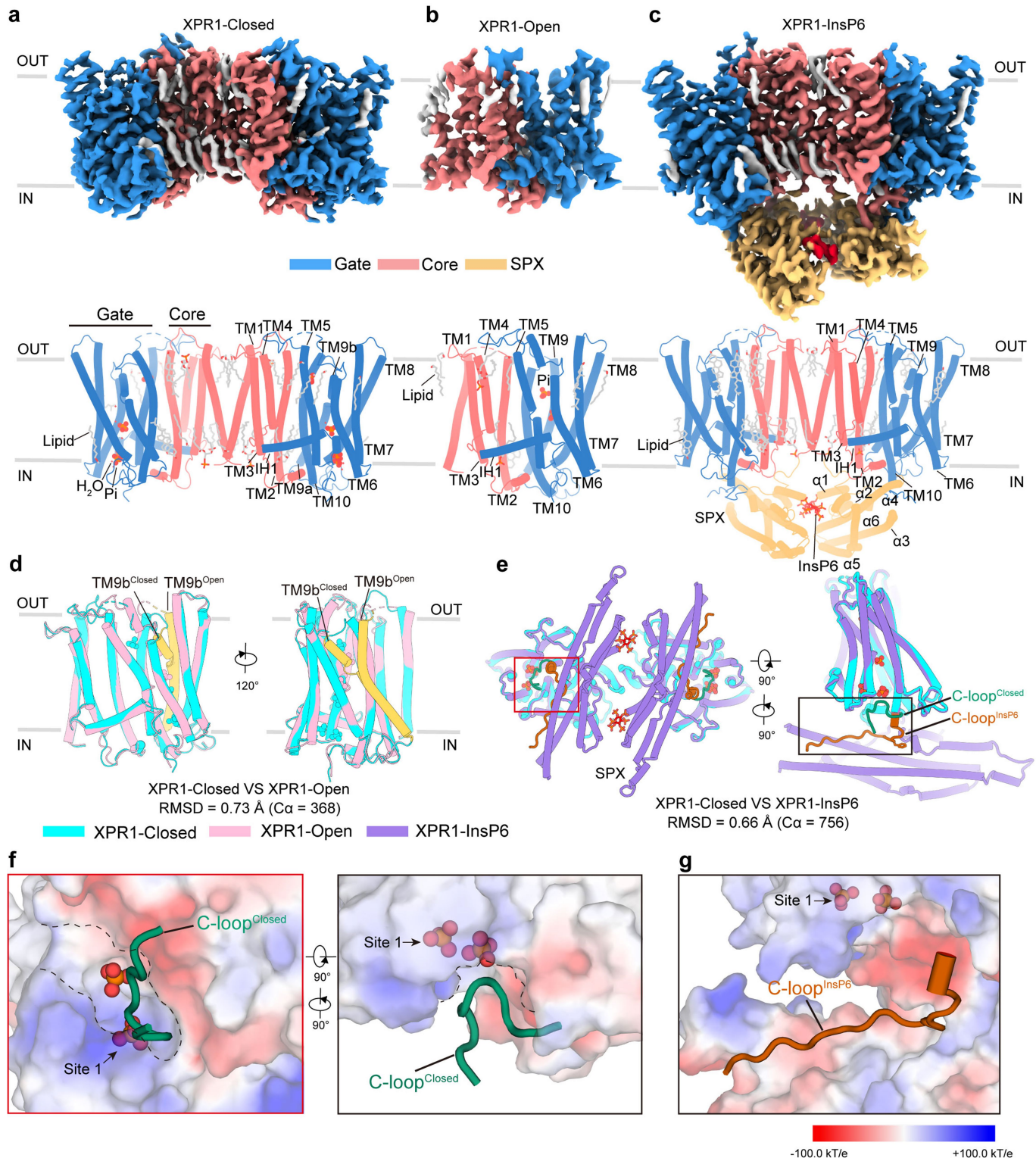
**Extended Data Fig. 4 | Cryo-EM data processing of XPR1<sup>InsP6</sup>.** **a**, The flowchart for cryo-EM data processing of XPR1<sup>InsP6</sup>. A representative motion-corrected electron micrograph (out of 2,800 micrographs) of XPR1<sup>InsP6</sup>. Scale bar, 50 nm. Scale bar in reference-free 2D class averages is 10 nm. **b**, Local resolution distribution map of XPR1<sup>InsP6</sup>. **c**, Particle angular distribution of XPR1<sup>InsP6</sup>.

**d**, FSC analysis of XPR1<sup>InsP6</sup>. The FSC curves of the final EM map without and with a solvent mask are colored in blue and red, respectively. Red arrow indicates the resolution of the map when FSC = 0.143. The FSC curve of the refined model fitting in the final EM map is colored in black. Black arrow indicates the resolution of model-map fitting when FSC = 0.5.



**Extended Data Fig. 5 | Representative EM densities of XPR1.**  
**a–c.** Representative EM densities for TM helices of XPR1<sup>Closed</sup> (**a**) and XPR1<sup>Open</sup> (**b**) and for the C-loop (**c**) of XPR1<sup>Closed</sup> (upper) and XPR1<sup>InsP6</sup> (lower). **d**, EM densities for the potential Pi molecules bound in XPR1<sup>InsP6</sup> and XPR1<sup>Open</sup>. Densities for Pi and interacting residues are shown in green meshes. **e**, EM densities for the SPX

## Article

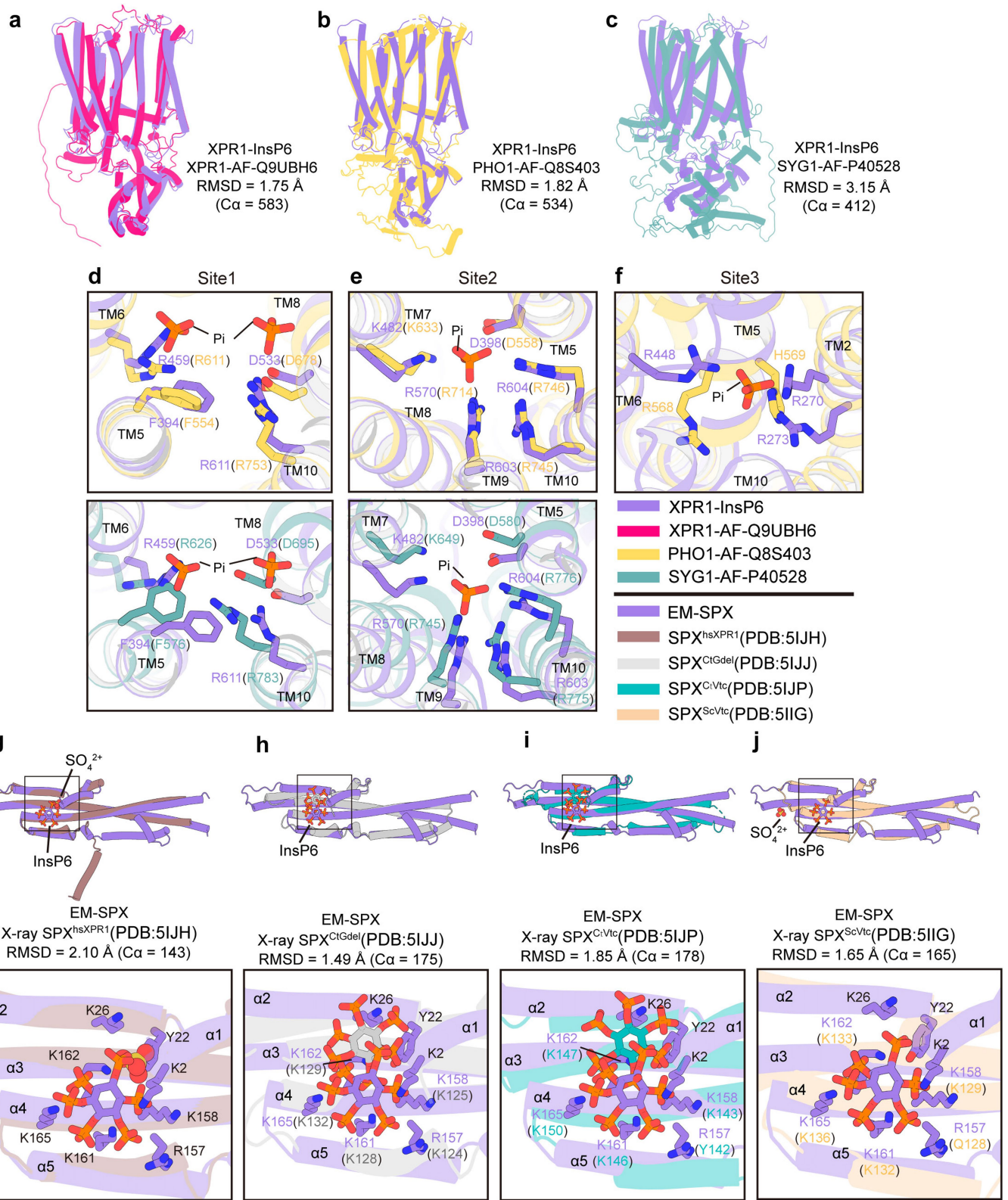


## Extended Data Fig. 6 | Structural comparisons of XPR1 in different states.

**a-c**, EM maps and cartoon representations of human XPR1 determined in closed (**a**), open (**b**), and InsP6-bound (**c**) states. The SPX, core, and gate domains are colored in yellow, red, and blue, respectively. Lipids and InsP6 are presented in gray and red sticks. Pi molecules are depicted in red spheres.

**d**, Superposition of XPR1<sup>Closed</sup> (cyan) and XPR1<sup>Open</sup> (pink). **e**, Superposition of

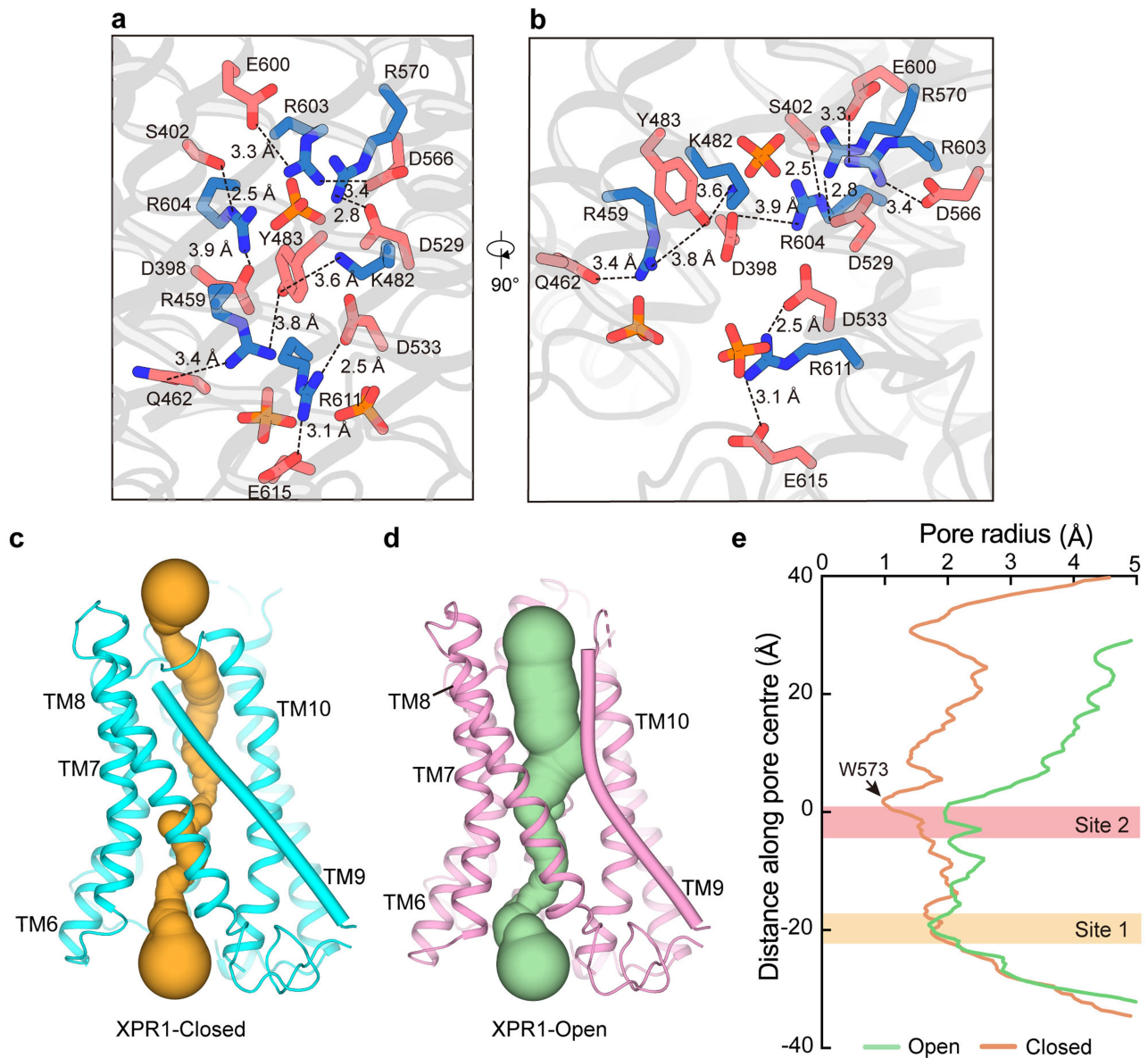
XPR1<sup>Closed</sup> (cyan) and XPR1<sup>InsP6</sup> (purple). The C-loop of XPR1<sup>Closed</sup> and XPR1<sup>InsP6</sup> are colored in green and orange, respectively. Red and black squares highlight the regions shown in panels f and g. **f,g**, Distinct positions of the C-loop in XPR1<sup>Closed</sup> (**f**) and in XPR1<sup>InsP6</sup> (**g**). The TMD and the SPX are shown in electrostatic potential surface. Phosphates are depicted in red spheres. The dashed black lines indicate the pathway for Pi accessing to Site 1.



#### Extended Data Fig. 7 | Structural comparisons of XPR1 homologs.

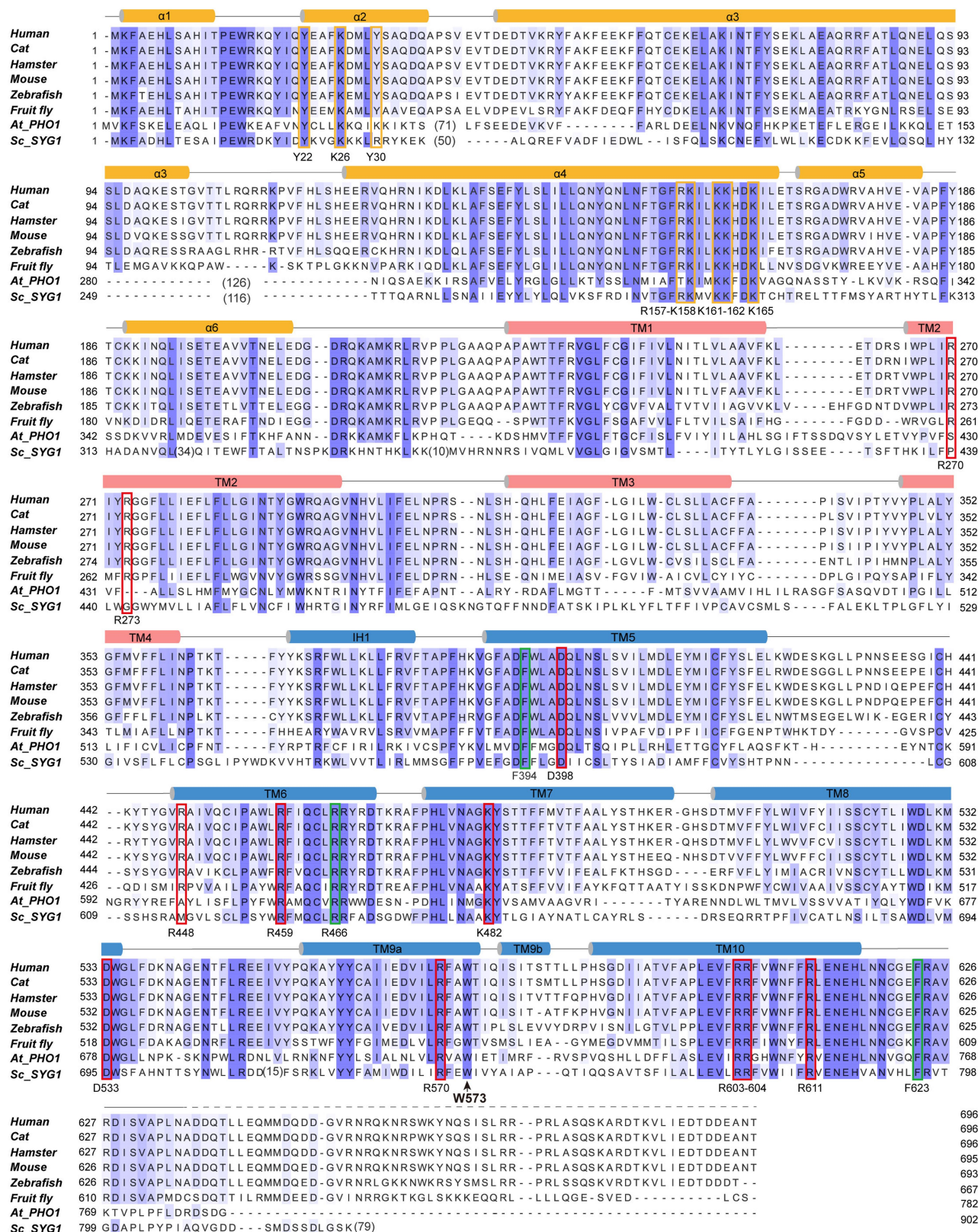
**a-c**, Superpositions of XPR1-InsP6 with the Alphafold2 models of human XPR1 (**a**), plant *A. thaliana* PHO1 (**b**) and yeast *S. cerevisiae* SYG1 (**c**). The EM structure of XPR1-InsP6, AF2 models of XPR1, PHO1, and SYG1 are colored in purple, red, yellow, and green, respectively. **d-f**, Comparisons of Pi binding Site1 (**d**), Site2 (**e**), and Site 3 (**f**) between the structure of XPR1-InsP6 (purple) and AF2 models of SYG1

(green) and PHO1 (yellow). **g-j**, Structural comparisons of the InsP6-bound SPX domain of XPR1-InsP6 with the X-ray structures of the isolated SPX domains of human XPR1 (**g**), *Chaetomium thermophilum* Gde1 (**h**), *Chaetomium thermophilum* Vtc4 (**i**), and *Saccharomyces cerevisiae* Vtc4 (**j**). The black squares indicate the InsPPs binding sites highlighted below.

**Extended Data Fig. 8 | The hydrophilic cavity and pore radius of XPR1.**

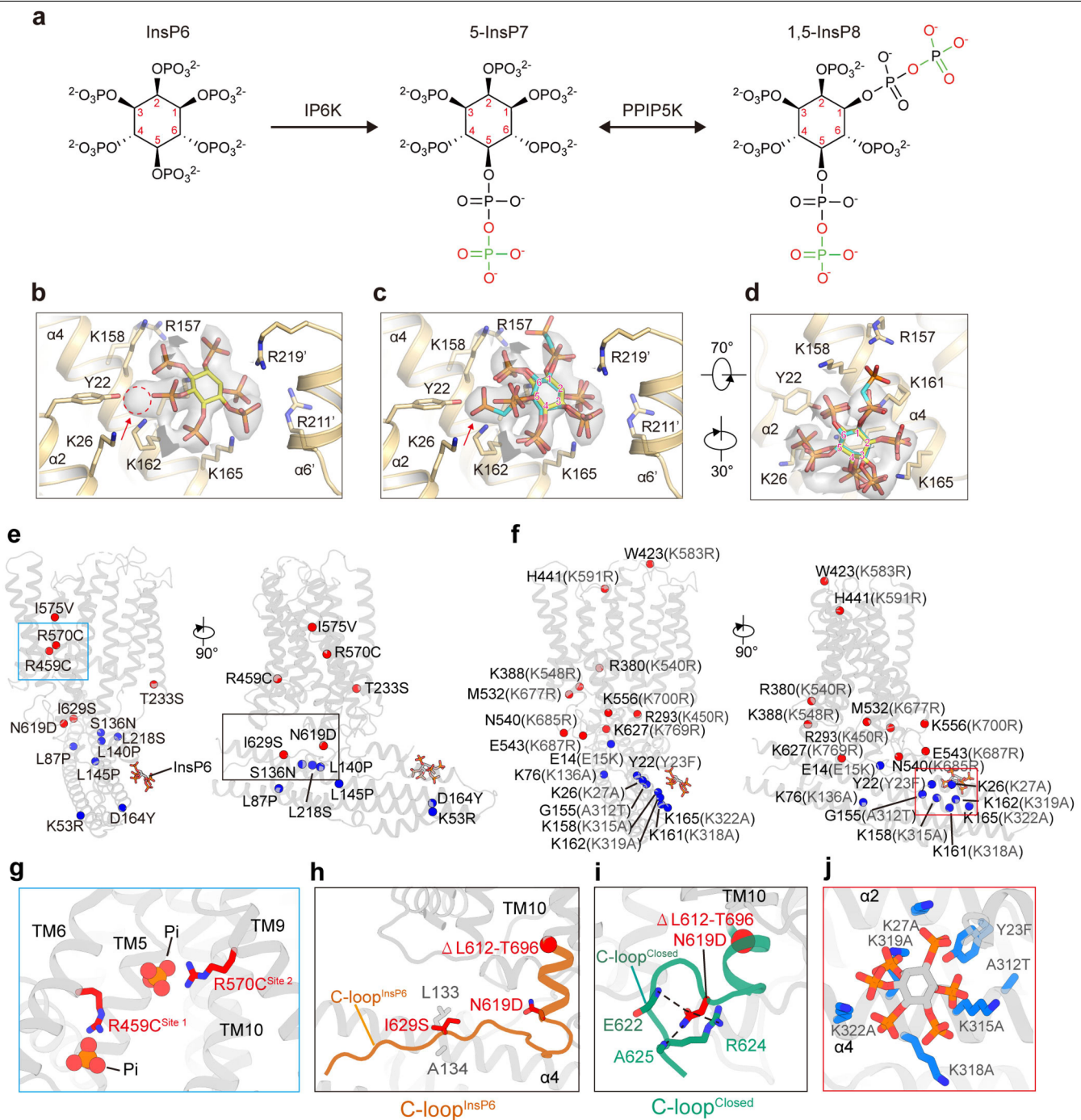
**a,b**, The basic clusters in Pi binding Sites 1 and 2 are balanced by multiple negatively-charged residues. Basic residues are shown in blue sticks, acidic and polar residues are shown in red sticks. Black dashed lines represent electrostatic interactions and hydrogen bonds. **c,d**, Ion path in the gate domain of

XPR1<sup>Closed</sup> (**c**) and XPR1<sup>Open</sup> (**d**) by HOLE. XPR1<sup>Closed</sup> and XPR1<sup>Open</sup> in cyan and pink, respectively. TM9 is depicted in cylinder. **e**, Pore radii of XPR1<sup>Closed</sup> and XPR1<sup>Open</sup>. Sites 1 and 2 are highlighted in yellow and light red, respectively. The position of W573 is indicated by a black arrow.



**Extended Data Fig. 9 | Sequence alignment of XPR1 homologs.** Sequence alignments of XPR1 from human, cat, hamster, mouse, zebrafish, fruit fly, and PHO1 from *Arabidopsis thaliana*, SYG1 from *Saccharomyces cerevisiae*. Secondary structural elements are labelled on the top of the sequences. The

# Article



**Extended Data Fig. 10 | Modelling of 1,5-InsP8 into XPR1 and pathogenic mutations.** **a**, Chemical structures and metabolic pathway of InsPPs. **b**, The binding site and EM density of InsP6 in XPR1. EM density is shown in white surface and contoured at  $5.5\sigma$ . InsP6 in yellow and red. Red arrow and red dashed circle indicates the extra density in the InsP6 binding site. **c,d**, Fitting of 1,5-InsP8 into the InsP6 site in XPR1 from different views. 1,5-InsP8 in cyan and red. **e,f**, Mutations causing PFBC (**e**) and mutations in PHO1 causing

reduced growth phenotypes (**f**) are mapped on the XPR1 structure. The blue and red spheres represent the mutations located in the SPX domain and the TMD, respectively. Blue, black and red squares indicate the regions shown in panels **g-j**. **g-j**, Zoom-in views of the pathogenic mutations in Pi binding sites (**g**), the C-loop of XPR1<sup>InsP6</sup> (**h**) and XPR1<sup>Closed</sup> (**i**), and InsP6 binding site (**j**). Pathogenic mutations of XPR1 and PHO1 are shown in red and blue sticks, respectively.

## Reporting Summary

Nature Portfolio wishes to improve the reproducibility of the work that we publish. This form provides structure for consistency and transparency in reporting. For further information on Nature Portfolio policies, see our [Editorial Policies](#) and the [Editorial Policy Checklist](#).

### Statistics

For all statistical analyses, confirm that the following items are present in the figure legend, table legend, main text, or Methods section.

n/a Confirmed

- The exact sample size ( $n$ ) for each experimental group/condition, given as a discrete number and unit of measurement
- A statement on whether measurements were taken from distinct samples or whether the same sample was measured repeatedly
- The statistical test(s) used AND whether they are one- or two-sided  
*Only common tests should be described solely by name; describe more complex techniques in the Methods section.*
- A description of all covariates tested
- A description of any assumptions or corrections, such as tests of normality and adjustment for multiple comparisons
- A full description of the statistical parameters including central tendency (e.g. means) or other basic estimates (e.g. regression coefficient) AND variation (e.g. standard deviation) or associated estimates of uncertainty (e.g. confidence intervals)
- For null hypothesis testing, the test statistic (e.g.  $F$ ,  $t$ ,  $r$ ) with confidence intervals, effect sizes, degrees of freedom and  $P$  value noted  
*Give  $P$  values as exact values whenever suitable.*
- For Bayesian analysis, information on the choice of priors and Markov chain Monte Carlo settings
- For hierarchical and complex designs, identification of the appropriate level for tests and full reporting of outcomes
- Estimates of effect sizes (e.g. Cohen's  $d$ , Pearson's  $r$ ), indicating how they were calculated

*Our web collection on [statistics for biologists](#) contains articles on many of the points above.*

### Software and code

Policy information about [availability of computer code](#)

Data collection All cryo-EM data were collected using EPU v3.1

Data analysis Collected cryo-EM data were processed using Relion 3.1, MotionCorr2 1.6.3, Gctf 1.3, cryoSPARC v4.1.0, Map and model refinement were processed with UCSF-Chimera v1.15, AlphaFold 2, COOT v0.9.2, Phenix v1.19. SEC-MALS results were analyzed using ASTRA v6.1. All figures were analyzed and made using Pymol v2.4.0, ChimeraX v1.1, Excel2019, Jalview1.8.3 and Graphpad v8.0.2.

For manuscripts utilizing custom algorithms or software that are central to the research but not yet described in published literature, software must be made available to editors and reviewers. We strongly encourage code deposition in a community repository (e.g. GitHub). See the Nature Portfolio [guidelines for submitting code & software](#) for further information.

### Data

Policy information about [availability of data](#)

All manuscripts must include a [data availability statement](#). This statement should provide the following information, where applicable:

- Accession codes, unique identifiers, or web links for publicly available datasets
- A description of any restrictions on data availability
- For clinical datasets or third party data, please ensure that the statement adheres to our [policy](#)

The UniProt accession codes are Q9UBH6 (*Homo sapiens XPR1*) [<https://www.uniprot.org/uniprotkb/Q9UBH6>], Q8S403 (*Arabidopsis thaliana PHO1*) [<https://www.uniprot.org/uniprotkb/Q8S403>], P40528 (*Saccharomyces cerevisiae SYG1*) [<https://www.uniprot.org/uniprotkb/P40528>]. The PDB coordinates used for

structural alignments are 5IJH (SPX of human XPR1) [<http://doi.org/10.2210/pdb5IJH/pdb>], 5IJJ (SPX of Chaetomium thermophilum Gde1) [<http://doi.org/10.2210/pdb5IJJ/pdb>], 5IJP (SPX of Chaetomium thermophilum Vtc4) [<http://doi.org/10.2210/pdb5IJP/pdb>], 5IIG (SPX of Saccharomyces cerevisiae Vtc4) [<http://doi.org/10.2210/pdb5IIG/pdb>]. The three-dimensional cryo-EM density maps of human XPR1Open, XPR1Closed, and XPR1InsP6 have been deposited into the Electron Microscopy Data Bank under accession numbers EMD-38067 [<https://www.emdataresource.org/EMD-38067>], EMD-38065 [<https://www.emdataresource.org/EMD-38065>], and EMD-38068 [<https://www.emdataresource.org/EMD-38068>], respectively. The coordinates of human XPR1Open, XPR1Closed, and XPR1InsP6 have been deposited into the Protein Data Bank under accession codes 8X5E [<http://doi.org/10.2210/pdb8X5E/pdb>], 8X5B [<http://doi.org/10.2210/pdb8X5B/pdb>], and 8X5F [<http://doi.org/10.2210/pdb8X5F/pdb>], respectively. Source Data are provided with this paper.

## Research involving human participants, their data, or biological material

Policy information about studies with [human participants or human data](#). See also policy information about [sex, gender \(identity/presentation\), and sexual orientation](#) and [race, ethnicity and racism](#).

Reporting on sex and gender	N/A
Reporting on race, ethnicity, or other socially relevant groupings	N/A
Population characteristics	N/A
Recruitment	N/A
Ethics oversight	N/A

Note that full information on the approval of the study protocol must also be provided in the manuscript.

## Field-specific reporting

Please select the one below that is the best fit for your research. If you are not sure, read the appropriate sections before making your selection.

Life sciences       Behavioural & social sciences       Ecological, evolutionary & environmental sciences

For a reference copy of the document with all sections, see [nature.com/documents/nr-reporting-summary-flat.pdf](https://nature.com/documents/nr-reporting-summary-flat.pdf)

## Life sciences study design

All studies must disclose on these points even when the disclosure is negative.

Sample size	Statistical methods were not used to determine sample size. For cryo-EM analysis, the number of micrographs was determined by the availability of microscope time and the particle density on the grids. The cryo-EM data were collected until the reported high-resolution EM maps achieved. For functional assays, the sample sizes were 6–9 cells from at least three independent repeats, three independent repeats are commonly required for functional assay; and for each repeat, cells from 2 or 3 different dishes were used to reach a balance between statistical robustness and practicality.
Data exclusions	For cryo-EM analysis, micrographs with CTF fitting worse than 4-angstrom were discarded. Subsequent cryo-EM data processing only kept high-resolution and homogeneous particles to generate the final high-resolution maps.
Replication	Sample preparation related experiments including protein purification and SDS-PAGE analyses, were conducted at least three times. Despite some degree of variability in protein yields, the profiles of size-exclusion chromatography and SDS-PAGE were reproducible. Functional experiments were repeated at least three biological independent times, consistently yielding comparable results and reproducibility.
Randomization	Randomization was not used in this study because the specific types of the experiments conducted in this study do not necessitate it; they are not influenced by the sample allocation processes common in other research methods.
Blinding	Blinding was not used in this study because the subjective analysis was not needed. Each experiment was analyzed using consistent methods. Quantitative measurements using various approaches as described in the methods minimized biased assessment.

## Reporting for specific materials, systems and methods

We require information from authors about some types of materials, experimental systems and methods used in many studies. Here, indicate whether each material, system or method listed is relevant to your study. If you are not sure if a list item applies to your research, read the appropriate section before selecting a response.

**Materials & experimental systems**

n/a	Involved in the study
<input checked="" type="checkbox"/>	Antibodies
<input type="checkbox"/>	Eukaryotic cell lines
<input checked="" type="checkbox"/>	Palaeontology and archaeology
<input checked="" type="checkbox"/>	Animals and other organisms
<input checked="" type="checkbox"/>	Clinical data
<input checked="" type="checkbox"/>	Dual use research of concern
<input checked="" type="checkbox"/>	Plants

**Methods**

n/a	Involved in the study
<input checked="" type="checkbox"/>	ChIP-seq
<input checked="" type="checkbox"/>	Flow cytometry
<input checked="" type="checkbox"/>	MRI-based neuroimaging

**Eukaryotic cell lines**Policy information about [cell lines and Sex and Gender in Research](#)

Cell line source(s)	Sf9(Invitrogen, USA), HEK293F (FreeStyle 293F cells, Gibco, USA); HEK293T (Gibco, USA)
Authentication	Cell lines were verified by the manufacturers' websites. The cell lines were frequently inspected by their morphological features.
Mycoplasma contamination	The cell lines were not tested for mycoplasma contamination.
Commonly misidentified lines (See <a href="#">ICLAC</a> register)	None of the cell lines used is listed in the database of commonly misidentified cell lines maintained by ICLAC.

**Plants**

Seed stocks	N/A
Novel plant genotypes	N/A
Authentication	N/A